

Small-Scale Absorbed Dose Modelling in Selective Internal Radiation Therapy

Microsphere Distribution in Normal
Liver Tissue

Jonas Högberg

Department of Radiation Physics
Institute of Clinical Sciences
Sahlgrenska Academy at University of Gothenburg



UNIVERSITY OF GOTHENBURG

Gothenburg 2015

Cover illustration: Left: Large microsphere cluster in portal tract of normal liver of Pt 2, image produced by Johan Mölne; Upper right: Autoradiogram of normal liver of Pt 2, autoradiography performed by Jonas Högberg; Lower right: Simulation of geometrical absorbed dose distribution by branching artery tree model, image produced by Peter Bernhardt

Small-Scale Absorbed Dose Modelling in Selective Internal Radiation Therapy

© Jonas Högberg 2015
jonas.hogberg@radfys.gu.se

ISBN 978-91-628-9426-9

Small-Scale Absorbed Dose Modelling in Selective Internal Radiation Therapy

Microsphere Distribution in Normal Liver Tissue

Jonas Högberg

Department of Radiation Physics, Institute of Clinical Sciences
Sahlgrenska Academy at University of Gothenburg
Göteborg, Sweden

ABSTRACT

Radioembolisation (RE), with yttrium-90 (^{90}Y) labelled microspheres, is an increasingly common treatment method for unresectable liver tumours. The tolerable mean absorbed dose for normal liver (NL) tissue is higher in RE than in External Beam Radiation Therapy (EBRT); absorbed dose heterogeneity is thought to be one important reason, together with a low absorbed dose rate, but the knowledge of microsphere distributions is limited. The aim of this thesis was to describe macroscopic and small-scale heterogeneity in the distribution of microspheres and consequently in absorbed dose, and to create a hepatic branching artery tree model, able to reproduce normal liver microsphere and absorbed dose distributions. Another aim was to develop and evaluate a method for prediction of absorbed dose to the surgeon's hands during liver resection on still radioactive tissues.

Two patients with marginally resectable cholangiocarcinoma underwent resection, nine days after RE with resin SIR-Spheres[®]. Considering radiation safety, simulation of absorbed dose to surgeon's hands was performed with the software Varskin Mod 2[®] before surgery and absorbed dose rate measurements were done with thermoluminescent dosimeters (TLD) on resected tissue. The macroscopic sphere distribution within NL was investigated by gamma well chamber activity measurements on punch biopsies from sliced resected tissues and by calculating coefficient of variation (CV) and skewness (SK), in relation to biopsy mass. Small-scale heterogeneity in microsphere and absorbed dose distribution was studied by light microscopy and subsequent absorbed dose simulations by beta dose point kernel convolution. A branching artery tree model was used, to simulate microsphere and absorbed dose distributions.

Tissue measurements and simulations of absorbed dose to surgeon's hands showed similar results. The CV and SK of activity concentration, by gamma well chamber measurements, decreased rapidly with increasing mass and/or mean activity concentration. Aggregations of clusters increased in frequency and CV and SK for absorbed dose distribution increased with mean sphere concentration. The branching artery tree model was able to resemble the biopsy sphere and absorbed dose distributions.

Expected absorbed dose to the surgeon's hands was not alarming, but simulations and measurements of surgeon finger absorbed dose are recommended. Decreasing CV and SK for macroscopic distribution indicated a heterogeneous pattern larger than the punch biopsy masses investigated. Small-scale sphere and absorbed dose heterogeneity both increased with mean sphere concentration. The branching artery tree model helps to explain the distribution mechanism better than previous distribution models. The shown heterogeneity and the arterial tree model provide knowledge that may be helpful in optimising RE treatment, regarding number of injected spheres and activity per sphere.

Keywords: clusters, dosimetry, heterogeneity, liver, microspheres, radioembolisation, simulations, SIRT, surgery, yttrium-90

ISBN: 978-91-628-9426-9

SAMMANFATTNING PÅ SVENSKA

Radioembolisering (RE) genomförs på både primära levercancertumörer och metastaser där synlig tumörväxt är begränsad till enbart levern. Det vanligaste är att RE utförs på tumörer som inte är operabla, ibland med förhoppning om att de ska bli det. Metoden går ut på att mikrosfärer (diameter c:a 20 - 40 μm) av glas (Theraspheres®) eller hårdplast (resin) (SIR-Spheres®) förses med radioaktivitet, i form av β -strålaren yttrium-90 (^{90}Y) och sedan injiceras via leverartären, m h a kateter; mikrosfärerna pumpas av det naturliga blodflödet ut till framför allt levertumörerna och i begränsad utsträckning ut i normallevervävnaden. Mikrosfärernas storlek gör att de fastnar i de små blodkärlen, i tumörområdet och i levervävnaden. Medelräckvidden hos β -strålningen (elektronernas räckvidd) är endast 2,5 mm, vilket gör att bestrålningen begränsas till mikrosfärernas absoluta närhet, således främst till tumörvävnaden. Syftet är att tumörvävnaden ska hämmas av strålskadorna, samtidigt som angränsande normallevervävnad måste skonas från potentiellt livshotande strålskador.

Denna avhandling syftar till att beskriva hur ökad kunskap om stråldosfördelning i normal levervävnad, vid radioembolisering av levertumörer, kan bidra till förbättrade behandlingsmetoder och patientöverlevnad. De metoder som använts i de studier som avhandlingen baseras på är 1) autoradiografier (fotografering med strålningskänslig film) på utopererad, radioaktiv tumör- och levervävnad, 2) uppmätning av radioaktivitet i ett stort antal mindre vävnadsprover, 3) registrering av enstaka mikrosfärer och mikrosfäranhopningar (kluster) genom mikroskopi, 4) datorsimulering av mikrosfärfördelning i levern, samt 5) datorsimulering av stråldosfördelningar m a p nämnda mikrosfärfördelningar. Förutom detta har även stråldoser till fingrarna hos kirurger som opererar patienter med vävnader innehållande radioaktiva isotoper simulerats och stråldosmätningar gjorts på uttagen vävnad. Mätningar för att bedöma stråldosen till kirurgens fingrar stämde väl överens med simuleringar och visade inte alarmerande nivåer; försiktighet bör emellertid iakttas, varför simulering och mätning av stråldoser rekommenderas inför eventuell operation av RE-patienter.

Sammanfattningsvis, är tendens till klusterbildning och grad av stråldosheterogenitet i levernormalvävnaden större än vad tidigare forskning kunnat påvisa. Därigenom erhålls mer detaljerad kunskap om varför levern tolererar en högre medeldos från RE än från extern strålterapi. Dessa rön kan möjliggöra metodoptimering, exempelvis vid val av totalt antal injicerade mikrosfärer och mängden radioaktivitet per mikrosfär. Sammantaget påvisas en potential för förbättring av terapeutisk effekt och patientöverlevnad.

LIST OF PAPERS

This thesis is based on the following studies, referred to in the text by their Roman numerals.

- I. Högberg, J, Rizell, M, Hultborn, R, Svensson, J, Henrikson, O, Gjertsson, P, Bernhardt, P. Radiation exposure during liver surgery after treatment with ^{90}Y microspheres, evaluated with computer simulations and dosimeter measurements.
J. Radiol. Prot. 2012; 32: 439-446.
- II. Högberg, J, Rizell, M, Hultborn, R, Svensson, J, Henrikson, O, Mölne, J, Gjertsson, P, Bernhardt, P. Heterogeneity of microsphere distribution in resected liver and tumour tissue following selective intrahepatic radiotherapy.
EJNMMI Research 2014; 4:48.
- III. Högberg, J, Rizell, M, Hultborn, R, Svensson, J, Henrikson, O, Mölne, J, Gjertsson, P, Bernhardt, P. Increased absorbed liver dose in Selective Internal Radiation Therapy (SIRT) correlates with increased sphere-cluster frequency and absorbed dose inhomogeneity.
EJNMMI Physics 2015; 2:10.
- IV. Högberg, J, Rizell, M, Hultborn, R, Svensson, J, Henrikson, O, Mölne, J, Gjertsson, P, Bernhardt, P. A simulation model of microsphere distribution for selective internal radiation therapy agrees with observations
Submitted to The Journal of Nuclear Medicine.

RELATED PRESENTATIONS

1. Högberg, J, Gjertsson, P, Hultborn, R, Rizell, M, Henrikson, O, Himmelman, J, Bernhardt, P
Dosimetric aspects following radioembolization of liver with ^{90}Y microspheres
European Association of Nuclear Medicine (EANM), Munich, Germany; 10/2008, (Oral presentation)
2. Högberg, J, Rizell, M, Gjertsson, P, Himmelman, J, Bernhardt, P
Radiation protection considerations in surgery following radioembolization of liver with ^{90}Y microspheres
European Association of Nuclear Medicine (EANM), Munich, Germany; 10/2008, (Oral presentation)
3. Högberg, J, Gjertsson, P, Hultborn, R, Rizell, M, Henriksson, O, Nilsson, O, Svensson, J, Himmelman, J, Bernhardt, P
Analysis of resected hepatic tumor and normal tissues regarding heterogeneity in specific radioactivity following presurgical radioembolization with ^{90}Y resin microspheres
SNM Annual Meeting, Toronto, Canada; 06/2009, (Oral presentation)
4. Högberg, J, Rizell, M, Gjertsson, P, Hultborn, R, Henrikson, O, Svensson, J, Bernhardt, P
Bremsstrahlung imaging of ^{90}Y microspheres shows poor resemblance with distributions of $^{99\text{m}}\text{Tc}$ -MAA in liver
Molecular Imaging in Radiation Oncology (MIRO), Brussels, Belgium; 03/2010, (Poster presentation)
5. Högberg, J, Rizell, M, Gjertsson, P, Hultborn, R, Henrikson, O, Svensson, J, Bernhardt, P
On the dose heterogeneity in normal liver tissue due to treatment of liver tumors with yttrium-90 microspheres
25th Annual Congress on European Association of Nuclear Medicine, Milan, Italy; 10/2012, (Oral presentation)

CONTENT

ABBREVIATIONS	VI
DEFINITIONS IN SHORT	VIII
1 INTRODUCTION.....	1
1.1 Radiobiology and sphere distribution	4
1.1.1 Representativeness	4
1.2 Pre-clinical experience regarding microsphere distributions	6
1.3 Microsphere characteristics.....	7
1.3.1 Radionuclide properties.....	7
1.3.2 Microsphere types	7
1.4 Clinical background	8
1.4.1 Tumour response	8
1.4.2 Normal tissue complications	8
1.4.3 NTCP & TCP optimisation	9
1.4.4 Microsphere distribution heterogeneity.....	10
1.4.5 BED vs. absorbed dose.....	14
1.5 Imaging	14
1.5.1 Pre-therapeutic ^{99m} Tc treatment simulation	15
1.5.2 Post-therapeutic imaging.....	15
1.5.3 Correlation of pre-therapeutic imaging and clinical outcome	16
1.5.4 Pre- vs. post-therapeutic imaging	17
1.5.5 Future post-therapeutic imaging methods	17
1.5.6 Imaging limitations.....	18
1.5.7 Small-scale distribution and dosimetry	18
1.6 Computer models	18
1.7 Radiation safety and surgery	20
2 AIMS	23
2.1 Microsphere and absorbed dose distribution characteristics	23
2.2 Radiation safety during surgery	23

3	PATIENTS AND METHODS.....	27
3.1	Patients (I,II,III,IV)	27
3.1.1	Pre-therapeutic investigations	27
3.1.2	Radioembolisation.....	27
3.1.3	Surgery	28
3.2	Surgery radiation exposure (I)	28
3.2.1	Simulations.....	28
3.2.2	Measurements on resected tissue surface.....	29
3.3	Radioactivity in resected tissue (II, III).....	29
3.3.1	Activity and microsphere detection.....	29
3.3.2	Analysis of tissue activity heterogeneity	30
3.3.3	Simulation of absorbed dose (III).....	34
3.3.4	Statistics	34
3.4	Simulation of arterial tree model (IV).....	34
3.4.1	Microsphere distribution	34
3.4.2	Absorbed dose distributions	35
4	RESULTS	39
4.1	Pre-therapeutic imaging (I,II,III,IV)	39
4.2	Surgery radiation exposure (I)	39
4.3	Radioactivity in resected tissue (II,III).....	39
4.3.1	Autoradiography (II)	39
4.3.2	NL tissue activity distributions.....	40
4.3.3	NL tissue microsphere distributions.....	44
4.4	Arterial tree simulations (IV).....	48
4.4.1	Microsphere distribution	48
4.4.2	Absorbed dose distributions	51
5	DISCUSSION.....	55
5.1	Surgery radiation exposure (I)	55
5.2	NL tissue activity distributions (II,III).....	55
5.2.1	Macroscopic distribution.....	55

5.2.2	Small-scale distribution	56
5.3	Simulated absorbed dose (III)	57
5.4	Arterial tree model simulations (IV)	57
5.4.1	Microsphere distribution	57
5.4.2	Absorbed dose distribution.....	58
5.5	Clinical implications (II,III,IV).....	58
6	CONCLUSIONS	63
6.1	Surgery radiation exposure (I)	63
6.2	Microsphere distribution (II,III,IV).....	63
6.2.1	Macroscopic distribution (II).....	63
6.2.2	Small-scale distribution (II,III,IV)	63
6.2.3	Simulated distribution (IV).....	64
6.3	Absorbed dose distribution (III,IV).....	64
6.4	Clinical implications (II,III,IV).....	64
7	FUTURE PERSPECTIVES.....	69
	ACKNOWLEDGEMENTS	73
	REFERENCES	77

ABBREVIATIONS

^{90}Y	Yttrium-90
$^{99\text{m}}\text{Tc-MAA}$	Technetium-99m-labelled macro-aggregated albumin
ACV	Artery coefficient of variation (model parameter)
CPE	Charged particle equilibrium
CRC	Contrast recovery coefficient
CT	Computed tomography
EBRT	External beam radiation therapy
EMB	Embolisation (model parameter)
Gy	Gray, SI unit for absorbed dose 1 Gy = 1 Joule/kilogram
HDV	Hepatic tree distribution volume (model parameter)
HE	High energy
LE	Low-energy
LS	Lung shunting
MAD	Mean absorbed dose
ME	Medium energy
MRI	Magnetic resonance imaging
NL	Normal liver
NTCP	Normal tissue complication probability
PT	Portal tract(s) or Portal triad(s)
RE	Radioembolisation

REILD	Radioembolisation-induced liver disease
RILD	Radiation-induced liver disease
S/N	Signal-to-noise ratio
SBR	Signal-to-background ratio
SIRT	Selective internal radiation therapy
SPECT	Single-photon emission computed tomography
$T_{1/2}$	Physical half-life
TACE	Transarterial chemoembolisation
TCP	Tumour control probability
$TD_{5/5}$	Tolerance absorbed dose; risk of complication: 5% within 5 years
TLD	Thermoluminescent dosimeter
TNC	Tumour-to-normal-tissue activity concentration ratio

DEFINITIONS IN SHORT

Arteriole	Arterial vessel with inner diameter $< 100 \mu\text{m}$ This definition simplifies the cluster distribution description in this work. There is space for about 10 microspheres per cross-section in the largest arterioles, by this definition
Artery, small	Arterial vessel with inner diameter $\geq 100 \mu\text{m}$ This definition simplifies the description in this work
Cluster, <i>small</i>	2–19 spheres per cluster
Cluster, <i>medium</i>	20–49 spheres per cluster
Cluster, <i>large</i>	50–99 spheres per cluster
Cluster, <i>very large</i>	≥ 100 spheres per cluster
Heterogeneity, <i>large scale</i>	Resolution on a scale larger than 2 cm. Heterogeneity on this scale can be studied by external imaging methods. The considerable cross-dose between adjacent volumes on this scale is restricted to within a few millimeters at the sub-volume edges.
Heterogeneity, <i>macroscopic scale</i>	Resolution on a scale of 2.5–20 mm (equal to or longer than mean range of ^{90}Y beta dose point kernel). Structural heterogeneity in activity concentration cannot be effectively homogenised by cross-fire effects on a larger scale than this.

Heterogeneity,
small scale

Resolution on a scale of 1-2.4 mm (shorter than mean range of ^{90}Y beta dose point kernel). Regular variation on this scale or smaller will be more or less homogenised by cross-fire. Small-scale heterogeneity is interesting from a radiobiological perspective if the variation within a small volume is large enough to create absorbed dose gradients which are not homogenised, e.g. in presence of clusters.

Heterogeneity,
microscopic scale

Resolution on a scale < 1 mm. As the absorbed dose gradient is very strong close to deposits of microspheres, structural microscopic heterogeneity is expected to be present for isolated spheres. The cross-dose, i.e. cross-fire homogenisation effects between adjacent volumes, containing microspheres, will however be strong on this scale.

*“Imagination was given to man to compensate for what he is not,
and a sense of humour was provided to console him for what he is”*

-Oscar Wilde

1 INTRODUCTION

The liver is the most commonly affected organ by metastatic disease (Kuvshinoff and Fong 2007). It has been expected that up to 25% of all cancer patients will, sooner or later, develop hepatic metastases (Van de Wiele et al. 2012). Unfortunately, a minority of these patients are amenable to surgery, the only potentially curative treatment among those with colorectal metastases (Kuvshinoff and Fong 2007).

In a global perspective, primary hepatic cancer, mostly hepatocellular carcinoma (HCC), but also cholangiocarcinoma, is the second (men) and sixth (women) most common cause of cancer-related death, due to its high incidence in developing countries and low curability. Contributing factors to HCC are, mainly, chronic hepatitis (Type B and C), in developing countries. In developed countries, the causes are more related to alcohol-related cirrhosis and obesity-related fatty livers. A high incidence of cholangiocarcinoma, in Eastern Asia, is associated with liver fluke, but this cancer type is otherwise relatively rare (Jemal et al. 2011).

Surgery, and thus potential to cure, is possible only for a small minority of all primary and metastatic intrahepatic tumours. The options for prolonged survival are chemotherapy (Aljiffry, Walsh and Molinari 2009, Okada 1998, Lam et al. 2012) external beam radiation therapy (EBRT) (Fuss et al. 2004, Chen et al. 2010), including stereotactic (SBRT) (Jung et al. 2013, Mendez Romero et al. 2006) and intensity-modulated (IMRT) (Fuss et al. 2004) procedures, various ablation techniques (Kim et al. 2011, Minami and Kudo 2011) and different endovascular procedures; i.e. bland embolisation (Rand et al. 2005), transarterial chemoembolisation (TACE) (Llovet et al. 2002) and, the subject of this thesis, radioembolisation (RE) (Salem and Lewandowski 2013), also referred to as Selective Internal Radiation Therapy (SIRT) (Lau et al. 1998).

Standard EBRT is not very efficient, considering the high incidence of Radiation-induced liver disease (RILD), when optimising the absorbed dose necessary to obtain tumour response (Ingold et al. 1965, Fuss et al. 2004), albeit the results are improving, with modern EBRT techniques, mentioned above. Radioembolisation, on the other hand, seems to be a promising alternative, with low risk of toxicity (Riaz, Awais and Salem 2014), as compared to other palliative and, potentially, down-staging (Lau et al. 1998) methods mentioned above. Some reports are showing comparable (Kooby et al. 2010, Salem et al. 2010, Lance et al. 2011) and other better therapeutic outcome for RE (Salem et al. 2011, Lewandowski et al. 2009), as compared

to TACE, regarding time to T progression and risk of liver toxicity. This is interesting as TACE is often considered the standard treatment for HCC, in case of intermediate (stage B) disease (Bruix and Sherman 2011). A combination of RE and systemic chemotherapy has also shown promising results (Chua et al. 2011).

The pathophysiological background for liver RE and TACE is the dual blood supply of the liver, i.e. 1) the low-pressure hepatic portal venous system draining the guts and 2) the high-pressure arterial system of oxygenated blood, both ending in the sinusoids (capillaries) and drained by the central vein (Figure 1). The liver parenchyma obtains only $\frac{1}{4}$ of its blood supply from the artery and the rest from the portal system, while the tumors depend almost exclusively ($> 80\%$) on the arterial system (Kennedy et al. 2004). The background for this is not clear, but may be related to the increased interstitial fluid pressure of tumours causing a collapse of low-pressure vessels. By injecting the microspheres into the artery, the tumour-to-normal tissue activity concentration ratio (TNC) will thus typically be about 4 (Lau et al. 1998), but could at instances be as high as 25, for HCC tumours (Ho et al. 1998). $TNC < 2$, due to poor tumour vascularisation, is a contraindicator for RE (Lau et al. 2012), as the therapeutic index is too low (See section 1.5.1).

With three patients planned for neo-adjuvant therapy, including SIRT followed by surgery, at The Sahlgrenska University hospital, there was an opportunity to investigate the microsphere distribution in resected normal liver (NL) tissue. Generalisation of the results may be assumed, since the healthy liver tissue tends to be structurally similar for different individuals (see section 1.1.1). Contrary to normal liver, the structure, not least the vascular, of tumour tissues is extremely heterogenous, even within single tumour lesions. The focus of this work was on the normal liver tissue, to explore the background of the seemingly higher radiotolerance to internal radiation compared to EBRT. For this reason, this thesis is focused on the gathering of more information on the absorbed dose distribution in liver, following radioembolisation. Such information is crucial for the improvement of technical aspects of the treatment method and thereby an improved survival for these patients. In order to acquire this information, both computer simulations, as well as different kind of measurements were applied (see Patients and Methods).

Furthermore, a secondary focus, within the scope of this thesis, was to perform simulations of absorbed dose rate to the surgeons before resection procedure, as well as absorbed dose measurements on resected tissue, in order to validate the method (see Patients and Methods).

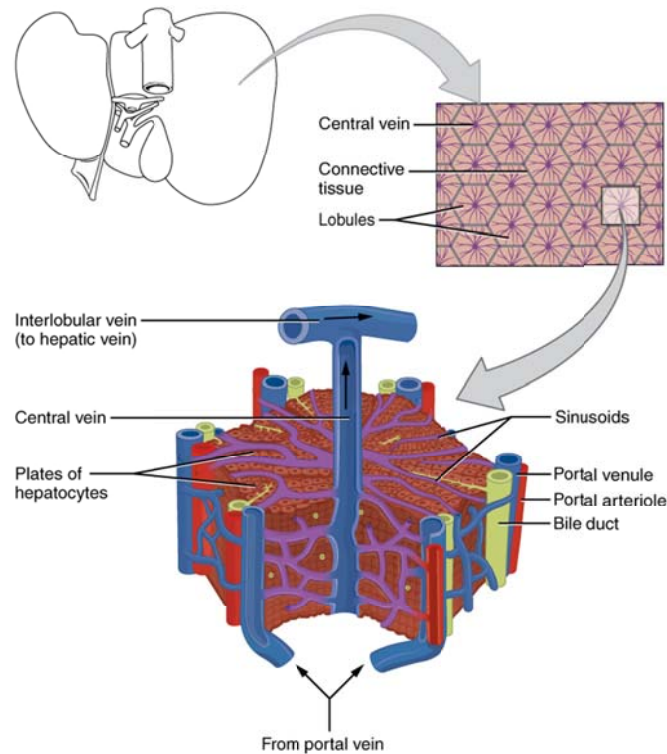


Figure 1. Liver microanatomy; the idealised, microscopic, hexagonal structure of the liver parenchyma, and the conceptual anatomy of a functional sub-unit, i.e. a liver lobule. The radius of a lobule, from the central vein and out, is 0.4 to 0.8 mm (Crawford, Lin and Crawford 1998); the shape may deviate (Debbaut et al. 2014) from the hexagonal ideal illustrated in the image. Furthermore, the image describes the organisation of portal tracts containing venules, arterioles and bile ducts, surrounding the lobule, but some portal tracts contain more than three vessels and ducts, not always occurring in multiples of balanced triads (Debbaut et al. 2014), as in the idealised image. The blood is flowing from the peripheral venules (portal system) and the arterioles (artery system), by the sinusoids (capillaries), passing by the hepatocytes (liver parenchyma cells), and is finally drained by the central vein and transported away to the hepatic vein.

Download image for free at <http://cnx.org/contents/14fb4ad7-39a1-4eee-ab6e-3ef2482e3e22@6.27/@6.27>.

1.1 Radiobiology and sphere distribution

In comparison to EBRT (See section 1.4.3), information on the radiation field, both within tumour and NL tissue, is limited in RE treatments. The treatment is simulated (see section 1.5.1) with an injection of technetium-99m-labelled macro-aggregated albumin (^{99m}Tc -MAA), followed by SPECT/CT (Single-Photon Emission Computed Tomography / Computed Tomography) imaging on the 140 keV gamma-radiation emitted by ^{99m}Tc . Several studies (see section 1.5.4) have shown that the actual distribution of the therapeutic agent, i.e. ^{90}Y -labelled microspheres, does not coincide well with simulations. Another challenge is the dependence on imaging per se; the distribution of microspheres could be evaluated post-therapeutically, with bremsstrahlung SPECT/CT and/or PET/CT (Positron Emission Tomography / CT). However, such non-invasive imaging methods are able to show only large-scale (> 2 cm) variations in ^{90}Y -distribution (see section 1.5.2).

1.1.1 Representativeness

Tumour tissue representativeness

Although the focus of this work is not on tumour tissue, some aspects making predictions for sphere distribution and thus absorbed doses will be briefly outlined.

The variation in morphology, considering tumour growth, is dependent on many parameters. In comparison to the highly organised normal vessels, the tumour vasculature is chaotic, with excessive branching and shunts, causing a high variability and unpredictability in blood flow (Carmeliet and Jain 2000, Tveit et al. 1987).

The vascular sprouting and growth towards a small tumour is radially organised, directed against the concentration gradient of the Vascular Endothelial Growth Factor (VEGF) (Ferrara, Gerber and LeCouter 2003). When entering the tumour tissue, the gradient of VEGF no longer exists, resulting in a haphazard vascular architecture with connections between immature capillaries with a poor and unpredictable blood flow. In larger tumours, an increasing interstitial fluid pressure will completely shut-down the perfusion in low-pressure vessels by vascular collapse. Furthermore, when considering tumour size, the variation in tumour characteristics, increases with volume, as larger tumours are more dependent on vascularisation (Milross et al. 1997, Lagerlöf, Kindblom and Bernhardt 2014). As larger tumours tend to suffer from insufficient vascularisation, a larger fraction of the central parts may suffer from hypoxia, leading both to potential regions of cell death (necrosis) and individual cells with hypoxia,

making them less sensitive to radiation (Kennedy et al. 2004). The combination of vascularisation characteristics, affecting the microsphere distribution, the fraction of necrotic and low-sensitive tissue, and how these tissue types are distributed geometrically, is thus unique for and within each lesion. The tendencies are correlated with tumour types (Leith et al. 1994) and size; however, as both size and individual characteristics of tumours differ, each patient is unique.

Thus great caution is needed in generalising data from a few or even many tumours (i.e. patients). In order to obtain fairly generalisable data, strict patient categorisation, based on tumour type and narrow tumour volume intervals, as well as other clinically important parameters, is necessary. Such categorisation requires large patient groups, in order to obtain large enough samples reflecting each category. Retrospective gathering of sufficient data, thus often requires multi-centre cooperation, with potential for inclusion-bias and lacking transparency for inter-centre methodologic differences and skills (Kennedy et al. 2009).

Normal liver tissue representativeness

Even though there is evidence of inter-individual, geometric, variation (Koops et al. 2004, Song et al. 2010) in the macroscopic artery structure of healthy liver tissue, it is obvious that liver parenchyma and its vascularisation is governed by genetic, organising rules (Carmeliet and Jain 2000), making different human livers resemble each other. With respect to microspheres, the distribution of the finest structures of the artery is crucial. The structure and function of the subunits of the liver differs between mammalian species, such as rats, pigs and humans, but within each species, e.g. humans, the characteristics are more constant. (Debbaut et al. 2014, Lamers et al. 1989, Crawford et al. 1998, Rappaport 1973, Rappaport et al. 1954, Teutsch 2005).

As there are large intra-individual variations (Debbaut et al. 2014) in the size and distribution of the small units (i.e. liver lobules), as well as in the size and distribution of liver vessels, it could be expected that the same kind of variation exists in all healthy human livers. The hepatic arterial system constitutes 19 – 21 artery generations (Walrand et al. 2014a, Debbaut et al. 2014), each generation with individual mean diameter as well as coefficient of variation (CV) for the diameter. If the mean variation within individuals (mean of all CVs), throughout different artery generations, is larger than the differences between individuals, concerning corresponding mean diameters, a large enough sample from one patient could be considered fairly representative for a patient population, even though some fractions of the distributions may not overlap between different individuals. The inter-individual similarities can be considered more striking than the differences, at

least on a microscopic level, as reported by Crawford et al. (Crawford et al. 1998), in comparing biopsies from 16 different patients. Given the supposedly genetically organised, albeit heterogenic and semi-randomised, fractal geometry principles ruling parenchyma and, probably, vessel structure (Crawford et al. 1998, Khokha, Landini and Iannaccone 1994), biopsies from healthy liver parenchyma ought to be reasonably representative, concerning the dynamic blood flow characteristics in arteries.

1.2 Pre-clinical experience regarding microsphere distributions

Distribution characteristics, regarding microsphere dimensions and number of injected spheres, were studied by Meade et al (Meade et al. 1987). They investigated how the distribution of microspheres, injected into rat livers, implanted with salivary adenocarcinoma tumour, varied with sphere size. The number of spheres injected was higher for smaller spheres. The reason for this was the aim for uniform sphere distributions in NL, while obtaining the highest TNC possible; they hypothesised that a relatively large number of the smallest spheres was needed, in order to obtain the same uniformity as for larger spheres. Comparing spheres of diameter 15, 32.5 and 50 μm , they found the 15 and 32.5 μm spheres to cause similar ratios (TNC 3.18 vs. 3.21) and higher than the 50 μm spheres (TNC 0.88). The CV for the distributions in NL decreased with sphere size, i.e. the distribution was more homogeneous for the larger spheres. It is notable, though, that the spheres were injected with ratios of 40:4:1 for 15, 32.5 and 50 μm , respectively. The tumour diameters varied from 4 to 10 mm, which corresponds to volumes of less than 0.6 cm^3 per tumour. Given the expected NL volume of about 12 cm^3 (Qin et al. 1990) and two tumours (one in each NL lobe), the tumour volumes would constitute less than 10% of NL volume. This means that the concentration ratios in NL would still be about 30:3:1, comparing the three sphere diameters. Care is therefore needed before concluding that the difference in CV for the NL distributions depends on size alone; it is possible that the CV dependence is explained by either sphere size, NL concentration or both.

1.3 Microsphere characteristics

1.3.1 Radionuclide properties

Yttrium-90 (^{90}Y) is a radioactive isotope of the rare-earth element yttrium (atomic number 39, stable isotope ^{89}Y). ^{90}Y decays, with half-life ($T_{1/2}$) 2.67 days, to stable Zirconium-90 (^{90}Zr) (atomic number 40) almost exclusively by β^- decay, resulting in the emission of a β -particle (electron), with a stochastically determined kinetic energy, within the nuclide-specific β -energy continuum. The ^{90}Y β -spectrum is relatively high-energetic, compared to most other β -emitters (Kassis and Adelstein 2005); the maximum and mean energies are 2.28 MeV and 0.934 MeV, respectively. The maximum and mean ranges of the β -particles (considering energy deposition distribution as described by the ^{90}Y beta dose point kernel) are 11 mm and 2.5 mm, respectively, in soft human tissue (Gulec et al. 2010) and the absorbed dose in relation to a homogeneous activity concentration, assuming charged particle equilibrium, is 49.8 Gy $\text{GBq}^{-1} \text{kg}^{-1}$ (Gulec et al. 2007). The CSDA range for the mean energy, 0.934 MeV, is 4.1 mm (Cremonesi et al. 2006). There is also a small probability (32×10^{-6}) of an alternative decay process, by internal electron & positron (e^- & e^+) pair production, by which ^{90}Y decays to the excited state of ^{90}Zr . The annihilation process of the emitted positrons can thus be examined with PET (Lhommel et al. 2009) (see section 1.5.2).

1.3.2 Microsphere types

Spheres labelled with ^{90}Y are manufactured as Theraspheres[®] by BTG, Ontario, Canada, (glass spheres) and as SIR-Spheres[®], by SIRTEx Medical Limited, Sydney, Australia, (resin spheres). The three main physical differences between glass and resin spheres, potentially making the distribution characteristics type-specific, are shown in Table 1.

The mean diameters do not differ extensively (Meade et al. 1987), but the glass spheres have a higher density and are therefore expected to be less compatible with the blood flow (higher aggregation probability) (Ho et al. 1998) and less comparable to the protein-based pre-therapeutic imaging particles ($^{99\text{m}}\text{Tc-MAA}$). Resin spheres, on the other hand, are more similar to protein, in density. The much higher specific activity, of glass- compared to resin spheres, shown in Table 1, is, however, compensated for, by a higher number of injected resin spheres vs. glass spheres.

Table 1. Comparison of reported physical characteristics for glass and resin spheres (Nelson, Vause and Koropova 2008, Cremonesi et al. 2014, Vente et al. 2009)

Type	Density (g/ml)	Diameter (μm)			Activity/sphere (Bq)
		Mean	Standard deviation	Span	
Glass	3.3	25	Not specified	20 – 30	2500
Resin	1.6	32.5	2.5	20 – 60	50

The number of glass spheres injected, per patient, is similar to the injected number of $^{99\text{m}}\text{Tc}$ -MAA particles at pre-therapeutic imaging, but the number of resin spheres injected is much higher. The high number of resin spheres therefore increases the tendency of aggregation and embolisation, although the spheres are more similar to the MAA particles. As both sphere types show promising therapeutic outcome, the two brands probably rely on different methodology, regarding distribution characteristics (see section 1.4.4).

1.4 Clinical background

1.4.1 Tumour response

As mentioned in the introduction, RE is continuously increasing as an adjuvant and alternative treatment for unresectable primary liver tumours and metastases confined to the liver. Albeit with slightly different physical properties (see section 1.4.2), both resin and glass spheres are successful in achieving a high TNC and are showing tumour response and prolonged patient survival outcomes, comparable to or higher than chemotherapy, not the least when RE and chemotherapy are combined. When treatment is successful it sometimes leads to down-staging (Lau et al. 1998) and enables surgery (see Introduction).

1.4.2 Normal tissue complications

There is still little knowledge about the radiation tolerance of NL tissue in RE, as it is hard to distinguish between administration-related and radiobiological complications (Kennedy et al. 2009) and furthermore, information about NL tissue absorbed dose is seldom available, especially for

glass spheres (Cremonesi et al. 2014). It is notable that the number of microspheres injected differs substantially, with a factor of 25 – 50 times higher for resin as compared to glass spheres. The different number of spheres per injection is reached by allocation of different activity per microsphere. It seems as if both tumours and NL have a higher tolerance for glass spheres, as higher MAD to tumour is needed for response, but also with seemingly less NL complications (Spreafico et al. 2014). It is hard to do conclusive comparisons, based on available clinical data, however, as determination of TNC (and thus the determination of administered absorbed dose to NL tissue) is not always considered necessary and, when performed post-therapeutically, the methods differ. (Cremonesi et al. 2014, Kao et al. 2011a, Riaz et al. 2011).

If the above assumption, about higher tolerance for glass spheres, is valid, it may be that this phenomenon depends on a less uniform absorbed dose distribution (see section 1.6) in both tumour and NL, for glass spheres (Walrand et al. 2014a). If the uniformity of absorbed dose, within NL, is more similar for the two sphere types than expected, however, there is an alternative possibility, that the higher incidence of complications for resin spheres depends more on administration failure, than on a more uniform absorbed dose distribution within NL, in general. It is important to identify patients with unfavourable vascularisation in tumour, as the resulting TNC otherwise may be too low, with a consecutive risk of a too high absorbed dose to NL (Kao et al. 2012). In that case, it is even possible that many complication-free patients may have been undertreated, as caution with the amount of administered activity may be influenced by maltreatments, due to lack of clinical information.

1.4.3 NTCP & TCP optimisation

A constant challenge in radiation therapy is the demand of minimising the normal tissue complication probability (NTCP) (Walrand et al. 2014b, Chiesa et al. 2012, Strigari et al. 2010), while maximising the tumour control probability (TCP), in order to kill the largest possible fraction of the tumour volume. The risk of liver failure in EBRT is calculated to be very low (< 5% within 5 years; $TD_{5/5}$), if the MAD in the semi-homogeneous (i.e. slow dose gradients present within major parts of NL) radiation field is kept below 30 Gy, for the whole liver treatment, and below 40 - 50 Gy in a treatment where only 1/3 of the NL is within the radiation field, (Milano, Constine and Okunieff 2007, Emami et al. 1991, Pan et al. 2010). The advantage in the treatment of the liver, being an organ with a repetitive functional structure (i.e. a parallel organ) (Källman, Ågren and Brahme 1992), is that a high

absorbed dose (up to 90 Gy) to outskirts of the NL does not imply failure of the entire organ (Pan et al. 2010, Dawson et al. 2002).

There are several pit-falls present in comparing EBRT to RE; the radiation field in EBRT could be considered semi-homogeneous, in comparison to the non-uniform field that may be present within a microsphere distribution. In an ideal situation, with perfect knowledge of the radiation field, it would be tempting to compare dose-volume histograms from EBRT with RE. Caution is needed in doing such comparisons, though, as the spatial distribution is expected to be different, with slow-gradient fields in EBRT and a high number of distributed point sources in RE. Not yet considering the range of the radiation in RE and thus the extent of crossfire, it is still reasonable to think that tissue structures distributed close to lodging sites of microspheres are expected to suffer more from these points sources than tissue structures distributed farther from such sites.

1.4.4 Microsphere distribution heterogeneity

As mentioned in section 1.4.2, the number of microspheres injected seems to have a high impact on the level of resulting heterogeneity in both sphere and absorbed dose distributions. The ideal treatment would of course be limited to the tumour tissue (infinite TNC). This is not possible in practice, but an important aim is to achieve a high TNC and a low absorbed dose to NL. Typically, the TNC is within the span of 2 – 7 for metastases (e.g. colorectal cancers), but the variation tends to be even higher in treatment of HCC (Ho et al. 1997).

Particle range considerations

When the distribution of the therapeutic radionuclide is expected to be fairly homogeneous, and/or when the tumours are considered small, a radionuclide with a low (α -emitters, range $< 100 \mu\text{m}$) or medium range (low energy β -emitters, mean range $< 1 \text{ mm}$) is the best choice, in order to obtain a low absorbed dose to healthy tissue, surrounding the tumour. When the radionuclide distribution is expected to be heterogeneous (due to tumour size or heterogenic structure, e.g. for unresectable liver tumours), it is preferable to use a radionuclide that is able to homogenise the heterogeneous distribution, thereby obtaining a more uniform absorbed dose distribution, thanks to so called crossdose by crossfire effects (Kassis and Adelstein 2005). However, the mean range of the β -radiation is only 2.5 mm (see section 1.3.1). As mentioned in section 1.6, the absorbed dose drops of by a factor 100 in just 1 mm (Gulec et al. 2010). Given that a cube has eight corners, the centre in a unit cube in a homogeneous single sphere pattern of unit size 2.5 mm will receive the major absorbed dose contribution from

eight close spheres, the sum being only a few percent of the self-absorbed dose for a $0.5 \times 0.5 \times 0.5 \text{ mm}^3$ voxel, containing a microsphere. The total absorbed dose contribution from the next shell of $64 - 8 = 56$ spheres is also only a few percent; the total contribution from the next shell of $216 - 64 = 152$ spheres is even less, as well as from the fourth shell of $512 - 216 = 296$ spheres. The maximum range of 11 mm means that a maximum of four shells will influence the absorbed dose. As the contribution from each of these shells is only a few percent, it is fair to assume that heterogeneity on a scale of 2.5 mm (or even smaller) will not be homogenised by cross-fire. A cube with side 2.5 mm has a mass of $2.5 \times 2.5 \times 2.5 = 16 \text{ mg}$, assuming density 1.0 g cm^{-3} .

Normal liver parenchyma vs. tumour tissue

Heterogeneity in absorbed dose distribution, following RE, causing cold spots of low absorbed dose within tumour tissue will not be beneficial from a tumour killing perspective. Within NL tissue, on the other hand, such cold spots will increase the probability of parenchyma survival. As mentioned in section 1.1.1, the characteristics of tumour tissue and NL parenchyma, including vascularisation, are very different. NL parenchyma, being governed by fractal geometry principles by genetic rules, is expected to possess higher levels of organised complexity, regularity and predictability than tumour tissue, the latter being more chaotic (and thus with a less generalisable character).

The implication of this is that, even though heterogeneities are found both within NL tissue and tumour tissue, the heterogeneity within the two tissue types could not be expected to be similar, even though it is not impossible. Even in the therapeutically non-ideal situation of a TNC close to 1 (similar microsphere concentration in both tissues), the intrinsic microsphere distributions could not be assumed to be similar, comparing the two tissue types.

In case of a sufficiently high TNC, a fairly uniform absorbed dose distribution (due to a high sphere concentration) within tumour tissue may still be accompanied by substantial absorbed dose non-uniformity within NL tissue, which would be favourable, from a therapeutic, radiobiological point of view. On the other hand, it is possible that a non-uniform absorbed dose distribution in tumour will be accompanied by a quasi-uniform absorbed dose distribution in NL. The latter case would of course not be optimal from a therapeutic point of view, unless the TNC is very high.

Therefore, important aims are to investigate i) the degree of heterogeneity in the NL microsphere distribution, ii) the absorbed dose distribution within NL,

following RE therapy, and iii) the relationship between these non-uniformities and the local mean microsphere concentration (See Aims).

Locally absorbed dose in normal liver tissue

As microspheres are lodging in the smaller arteries and arterioles in the portal tracts (PT), (also called portal triads, referring to their idealised structure, as illustrated in Figure 1), the absorbed dose distribution for PT could be expected to have a higher MAD than the total parenchyma volume. Very few spheres can pass through the capillaries over to the central vein, within NL, and the total volume of central veins is thus expected to receive an even lower MAD (Gulec et al. 2010, Walrand et al. 2014a).

Cluster gatherings and small-scale dose distributions

The studies of small-scale microsphere distribution in NL tissue are few and limited regarding patient specific volume. Roberson et al (Roberson et al. 1992) studied and did dose simulations based on a small biopsy sample of rabbit NL and tumour tissue being injected with microspheres (polystyrene spheres, diameter 27 μm) and found a large variance in absorbed dose distribution in both tumour and NL. They reported cluster maximum sizes of 8 for NL and 13 for tumour and, furthermore, that the total relative variation (i.e. heterogeneity) in microsphere distribution was larger in normal than in tumour tissue. They admitted the need for a larger sample size in order to make conclusions about total NL distribution.

Pillai et al (Pillai et al. 1991) found even larger clusters (maximum sizes > 25 spheres per cluster) in rabbit NL and tumour tissue, using the same polystyrene microsphere type. For NL concentrations of 4.7 and 6.6 spheres/mg (corresponding to 12 and 17 Gy regions for resin spheres vs. 300-600 and 400-800 Gy regions for glass spheres), they found microsphere mean cluster sizes of 3.6 and 4.4 spheres per cluster, respectively; the clusters tended to be larger in tumour tissue, but primarily explained by large TNCs, as a TNC of 6 resulted in a similar mean cluster size as compared to NL and a TNC of 10 resulted in less than a doubled (factor 1.8) tumour mean cluster size. Given the high TNC in combination with a not very much larger mean cluster size for tumour tissue, the mean distance between clusters was four times higher in NL tissue (9.3 mm in NL vs. 2.5 mm in tumour), resulting in an expectedly more non-uniform D distribution in NL as compared to tumour, if using radiolabelling by β -emitters.

In a human study by Burton et al (Burton et al. 1989), one or a few biopsies of masses 1–10 g were collected from 9 patients and were sectioned into 2-51 0.1–0.2 mm sections per patient; the activity was then detected in a liquid scintillator. They found a large intra-biopic variance of the activity, described

with the coefficient of variation (CV); the variation between individuals was also high, however, as the CVs varied between patients: 0.31 to 1.6 in NL and 0.19 to 0.98 in tumour. Analysing some of their presented data, the CVs are found to have a negative correlation with absorbed dose (-0.4 for tumour and -0.5 for NL). The total volume investigated for each patient was small, however; it is possible that there is a large macroscopic variation throughout the liver, but the correlations suggests that there may be a tendency of decreasing microsphere heterogeneity with increasing MAD for both NL and tumour. As no three-dimensional small-scale investigation was made, little can be said about the distribution within individual thin sections from this study.

Fox et al (Fox et al. 1991) analysed a small volume of NL tissue and found a highly heterogeneous absorbed dose pattern.

There have been some reports (Kennedy et al. 2004, Campbell, Bailey and Burton 2000) on cluster gatherings in tumour tissue, studied in explanted tissue, treated some time before dissection. Kennedy et al reported, after dissection of four explanted livers, that both glass and resin microspheres caused high MAD regions, with heterogeneous microsphere aggregation patterns. Not much information is reported about intentions to track clusters in three dimensions; the clusters found for resin spheres were however larger (up to 20 spheres) compared to clusters of glass spheres (up to 4 spheres), probably explained by the 50 times lower activity per resin sphere as compared to glass spheres, and thus a higher total number of injected resin spheres, as the total injected activities were similar (3 GBq for resin- vs. 5 GBq for glass spheres). The TNCs were considerably higher for glass spheres, but the clinical value of this comparison is questionable, given the low number of patients (low representativeness for tumour tissue, as mentioned in section 1.1.1) and the tumour / sphere type specific relationship; the two patients receiving resin sphere treatment suffered colon metastases and the two glass sphere patients suffered HCC.

It is still notable that higher TNC for glass spheres (both TNCs > 6) did not result in a higher fraction of tumour volume destruction (detected as necrosis or fibrosis) than for resin spheres (both TNCs < 3). The reason for this may be coincidental, but it may also be that the radiation field, caused by glass spheres, tends to be more heterogeneous, given the much lower number of glass, as compared to resin spheres, and the stronger absorbed dose gradient in the vicinity of glass spheres, caused by higher activity per sphere.

1.4.5 BED vs. absorbed dose

Biological Effective Dose (BED), explained by the linear-quadratic (LQ) absorbed dose effect formalism (Dale 1985), is a common term within EBRT (Dale and Jones 2007), in order to account for absorbed dose rate and absorbed dose fractioning effects. Cremonesi et al (Cremonesi et al. 2008) applied the BED formalism on RE, when investigating the potential benefit of multi-cycle treatment in RE. They showed that BED to NL could be kept constant, independent of number of treatments (1 RE to 1/1 liver; 2 REs to 1/2 liver or 3 REs to 1/3 liver) as absorbed dose increased slightly for NL and both absorbed dose and (more importantly) BED increased for tumour, with expected better outcome for RE therapy. Other authors (Strigari et al. 2010) have also opted to explain clinical outcome of RE by NTCP and TCP models, including BED formalism. Non-uniformity is also treated by inclusion of the concept of Equivalent uniform BED (EUBED); it is notable, however, that different end points are compared, as the critical tissue in EBRT (with quasi-homogeneous D distribution in NL) is the central vein (risk for RILD) and in RE the hepatic arteries of the PT (risk for RE-induced liver disease, REILD) (Cremonesi et al. 2014). The reason for this difference is the mentioned lodging of microspheres within the arteries and arterioles in the PT, and the consequences of this for the microscopic absorbed dose distribution (See section 1.6).

1.5 Imaging

In any radionuclide therapy, information about the patient-specific pre-therapeutic clinical situation is crucial, for a determination to be made on whether the patient complies with the prerequisites for the suggested therapy or not. In RE therapy, it is important to identify any considerable risk for extensive shunting of microspheres to the lungs, gut, pancreas etc., as this may cause under-treatment of tumour tissue, as well as severe radiation-induced complications in mentioned organs (Goin et al. 2005, Yip et al. 2004, Leung et al. 1995, Hamami et al. 2009). One way of gathering this information is to simulate treatment with ^{99m}Tc -MAA imaging (see section 1.5.1). Furthermore, such imaging can provide additional information about the expected TNC and thus the probability for tumour response by the planned treatment. It is also of clinical value to gather post-therapeutic information about the actual distribution of spheres and thereby the achieved radiation field in both tumour and NL tissue, in order to find possible relationships between distribution characteristics (e.g. TNC) and the outcome of the treatment (i.e. tumour response and patient population survival). Two possible post-therapeutic imaging techniques are i) SPECT (Ahmadzadehfar et al. 2011a) (see section 1.5.2), i.e. imaging of bremsstrahlung, emitted when

the β -radiation is losing kinetic energy within tumour and NL tissue, and ii) PET, by positron-electron pair annihilation (see section 1.3.1 and 1.5.2), caused by the, for ^{90}Y , very rare decay process of internal pair production (Lhommel et al. 2009). Both SPECT and PET are combined with CT or MRI for optimal anatomic information.

1.5.1 Pre-therapeutic $^{99\text{m}}\text{Tc}$ treatment simulation

In order for the risk of extra-hepatic complications to be minimised, pre-therapeutic simulations of therapy are vital. As 95% of the MAA particles have diameters of 10 to 100 μm (Gandhi et al. 2013) and more typically 15 to 30 μm (Gulec et al. 2007), the size of MAA is similar to that of both microsphere types (20 to 40 μm).

Planar imaging

Pre-therapeutic planar imaging of the $^{99\text{m}}\text{Tc}$ -MAA distribution is performed in order to rule out the risk of too much of the therapeutic activity ending up in the lungs (O'Doherty, Scuffham and Hinton 2011). In case of lung shunting (LS) of 10 – 20%, the total injected therapeutic activity of ^{90}Y spheres is lowered by 20 – 40%, for resin spheres, whereas therapy is avoided if $\text{LS} > 20\%$; for glass spheres no adaption is made, but therapy is avoided if $\text{LS} > 10\%$ (Cremonesi et al. 2014).

SPECT/CT

In order for three-dimensional information about the expected distribution of therapeutic spheres to be gathered, planar imaging of $^{99\text{m}}\text{Tc}$ -MAA is often complemented by subsequent SPECT/CT of the NL and tumour region (Hamami et al. 2009). Thereby the TNC, and absorbed dose to tumour and NL tissue, may be determined (Ho et al. 1997, Gulec et al. 2007). A mean $\text{TNC} < 2$ is considered a contra indication for therapy (Kao et al. 2013a, Lau et al. 2012, Lau et al. 1998), as the achievable tumour absorbed dose often is too low at this level (See Introduction).

1.5.2 Post-therapeutic imaging

^{90}Y bremsstrahlung SPECT

As the therapeutic radionuclide ^{90}Y emits high energy β -radiation, the energy loss of the β -radiation, in its interaction with human tissue, gives rise to a bremsstrahlung emission spectrum. These photons can be detected by SPECT, even though the wide energy spectrum implies new challenges, not present in quasi-mono-energetic $^{99\text{m}}\text{Tc}$ γ -radiation imaging; in order to achieve high enough signal, one may use a wide energy window, typically 55 – 285 keV (Shen et al. 1994b, Knesaurek et al. 2010, Ahmadzadehfar et al.

2011b). The most energetic bremsstrahlung photons, together with scattered ones, will cause too much collimator septal penetration, blurring the entire image, with use of a Low-Energy (LE) collimator. The use of a Medium-Energy (ME) or a High-Energy (HE) collimator (Knesaurek et al. 2010, Ahmadzadehfar et al. 2011b, Elschot et al. 2011) and filtering (Shen, DeNardo and DeNardo 1994a) techniques may enable imaging with a fair sensitivity, i.e. signal-to-background ratio (SBR), and spatial resolution (Shen et al. 1994b) (See also Section 1.5.5).

⁹⁰Y PET

Thanks to the low, but considerable, probability of internal pair production, by the alternative decay process (see section 1.3.1), high enough ⁹⁰Y activity concentration in tissue shortly after therapy enables PET/CT or PET/MRI. Sufficiently high resolution and signal-to-noise ratio (S/N) are obtainable with conventional time-of-flight scanning, by small adjustments in scanning and image reconstruction parameters (Lhommel et al. 2009, Kao et al. 2011b, Wissmeyer et al. 2011, Kao et al. 2013b).

Comparison of post-therapeutic imaging methods

The spatial resolution is better for ⁹⁰Y PET (9.3 mm) (Kao et al. 2013b) than for ⁹⁰Y bremsstrahlung SPECT (11 – 17 mm, depending on body/phantom depth of radioactive volume) (Elschot et al. 2011). In order to distinguish nearby volumes of similar or different activity, it is more interesting to compare contrast recovery coefficients (CRC) and its dependence on activity source diameter. A simplified description of CRC is: the ratio of measured vs. actual activity concentration ratio, where the activity concentration ratio refers to a smaller volume vs. a larger volume surrounding the smaller volume. PET has shown better CRC (ideally CRC = 100%) than parallel collimator bremsstrahlung SPECT. In a phantom with 10 times higher activity concentration in phantom spheres, compared to surrounding liquid, the CRCs were: SPECT: 25% vs. PET: 55%, for spheres with diameter 10 mm; for corresponding 37 mm spheres, the CRCs were: SPECT: 42% vs. PET: 89% (Elschot et al. 2013). SPECT is however a competitive alternative, considering imaging straightforwardness and cost-effectiveness (Walrand et al. 2011) (See also section 1.5.5).

1.5.3 Correlation of pre-therapeutic imaging and clinical outcome

Even though there are studies showing correlation between pre-therapeutic ^{99m}Tc-MAA-imaging TNC and tumour-response (Gulec et al. 2007, Flamen et al. 2008, Kao et al. 2012) there are also reports not able to show such correlation (Dhabuwala, Lamerton and Stubbs 2005, Haug et al. 2011). The

use of ^{99m}Tc -MAA SPECT (in comparison to only planar ^{99m}Tc -MAA imaging, for shunting examination) is however advisable, from a safety perspective, as SPECT is superior in identifying patients with increased risk for intra-hepatic or extra-hepatic radiation toxicity (Kao et al. 2013a, Ahmadzadehfar et al. 2010, Hamami et al. 2009) (see section 1.5.1).

1.5.4 Pre- vs. post-therapeutic imaging

The reason for ^{99m}Tc -MAA being a questionable predictor of tumour response is in line with reports, showing that i) catheter positioning and ii) unique physical properties of MAA may influence the distribution patterns, resulting in a poor correlation (Wongergem et al. 2013). Post-therapeutic PET (Haug et al. 2011, Kao et al. 2013b) and SPECT (Meyer et al. 2014, Ahmadzadehfar et al. 2014) imaging techniques are therefore often better indicators of tumour response and risk for complications. Given the actual benefits of pre-therapeutic images together with more reliable information obtainable by post-therapeutic imaging, the combination of both is highly desired.

1.5.5 Future post-therapeutic imaging methods

Some studies (Minarik, Sjogreen Gleisner and Ljungberg 2008, Rong et al. 2012) have shown the potential of improving CRC in bremsstrahlung imaging, by applying compensatory kernels for attenuation, scatter and collimator-detector effects in the reconstruction algorithm, but these methods are not yet clinically available. As PET is a more expensive imaging method than SPECT, Walrand et al (Walrand et al. 2011) presented a pinhole collimator SPECT system (increased CRC as compared to parallel collimator SPECT) as an alternative to PET imaging.

Another way of improving post-therapeutic imaging properties in RE is the use of spheres labelled with nuclides emitting both β - and γ -radiation, e.g. Rhenium-188 (^{188}Re) (Nowicki et al. 2014) and Holmium-166 (^{166}Ho) (Smits et al. 2012). The obvious advantage is the possibility to use more traditional (i.e. narrow energy window) SPECT techniques for post-therapeutic imaging, with almost perfect CRC. An additional advantage of ^{188}Re ($T_{1/2}$: 16.9 h; maximum β -energy: 2.12 MeV; γ -energy: 155 keV), over ^{90}Y , is the lower cost (^{90}Y is produced by chemical separation from the mother nuclide ^{90}Sr , common in fission product waste) (Kodina, Korpusov and Filyanin 2002) and higher availability, as ^{188}Re is produced in a generator, that can be set up in a hospital radiopharmacy, with the rather long-lived mother nuclide Tungsten-188 (^{188}W , $T_{1/2}$: 69 days) (Knapp et al. 1997). ^{166}Ho ($T_{1/2}$: 26.8 h; maximum β -energy: 1.84 MeV; γ -energy: 81 keV) distribution, on the other hand, is possible to examine with MRI, since holmium is paramagnetic (van de Maat

et al. 2013). ^{166}Ho is also generator-produced, without need to rely on access to accelerator or reactor (Uusijärvi et al. 2006). Even though the mentioned nuclides have similar energy properties and mean CSDA range (Mean CSDA range: ^{90}Y : 4.1 mm; ^{166}Ho : 0.9 mm and ^{188}Re : 3.8 mm), the therapeutic properties may still differ and need further clinical evaluations, as the absorbed dose rate, being different for the three radionuclides, is an important parameter (Hall and Brenner 1992, Cremonesi et al. 2006).

1.5.6 Imaging limitations

Low imaging spatial resolution (see section 1.5.2), compared to distribution heterogeneity and absorbed dose non-uniformity, makes available non-invasive imaging methods unable to describe the small-scale absorbed dose distribution. Therefore, smaller, but potentially frequent, low absorbed dose (“cold”) volumes within NL parenchyma, remain undetected with SPECT and PET. Knowledge of such cold volume distributions may be beneficial, for the development of a better NTCP model for RE, but methods, complementary to external imaging, are needed.

1.5.7 Small-scale distribution and dosimetry

Knowledge about small-scale distribution would add another dimension to the otherwise large-scaled data bank of absorbed dose distribution. Even though investigation of macroscopic and small-scale absorbed dose distribution (e.g. biopsy samples from treated patients) is not feasible on a regular basis, in-vivo, such knowledge, i.e. increase/decrease of heterogeneity with large-scale absorbed dose (the latter available by imaging) would be important clinical input. Such knowledge may justify the inclusion of e.g. a radiobiological correction factor for heterogeneity, as a function of absorbed dose. Increased knowledge of the relationship of microsphere concentration and aggregation tendency (cluster formation) may affect the optimisation of number of injected spheres and preferred activity per sphere. To provide information about small-scale sphere and absorbed dose distributions is one main objective of this thesis.

1.6 Computer models

Some computer models have been developed for microsphere as well as absorbed dose distributions, following RE, on a microscopic, small and macroscopic scale. Kennedy et al (Kennedy et al. 2010) developed a model, trying to describe the microsphere flow distribution through arterial branching nodes (bifurcations). Their model demonstrated that the distribution of microspheres, through different daughter vessels, did depend

on parameters such as vessel bifurcation geometry, shape of particle inlet distribution (uniform vs. parabolic) and pressure boundary conditions. Furthermore, authors from the same research team demonstrated, in another study (Basciano et al. 2010), that glass and resin spheres are expected to distribute in similar ways, despite their difference in physical characteristics.

Concerning absorbed dose distribution, Gulec et al (Gulec et al. 2010) simulated small-scale absorbed dose distribution (Stenvall et al. 2014), by Monte Carlo modelling, for various microanatomic structures surrounding deposited microspheres. In lack of clinical data, on true sphere distribution patterns, a uniform distribution was assumed, within the terminal arterioles of the portal triads. This model showed strong absorbed dose gradients; when crossfire was ignored, the adjacent PT artery, lodging a sphere, received an absorbed dose more than 100 times higher than the absorbed dose received by liver parenchyma residing > 1 mm from a sphere. Including cross fire effects, the ratio of the absorbed dose to parenchyma vs. to PT was 1:3. The consequence of the uniform sphere distribution was a lack of absorbed dose variance within the same structural category (e.g. PT), for high sphere concentrations, corresponding to resin sphere distributions. For low sphere concentrations, corresponding to glass sphere distributions, the ratio of absorbed dose to parenchyma vs. to PT varied between 1:1 and 1:5. This was due to the number of spheres being lower than the total number of PT, leaving only one sphere in every other portal tract. According to this model, a lower number of spheres may be beneficial, with a larger fraction of the total PT volume receiving a moderate absorbed dose.

Walrand et al (Walrand et al. 2014a) considered the outcome of the mentioned models (Kennedy et al. 2010, Gulec et al. 2010) and constructed an extended model, including non-uniform distributions of microspheres and absorbed dose. Non-uniformity was obtained by the assignment of uneven relative spreading probability throughout the vessel bifurcations of a virtual branching artery tree model, with 21 branching nodes. The effect of non-uniformity was larger for a low number of injected spheres, corresponding to typical concentrations for glass sphere RE, as compared to the higher sphere concentration for resin spheres. This is in harmony with the hypothesis of a higher tolerance for glass as compared to resin spheres, mentioned in section 1.4.2 and in the above paragraph. They also performed NTCP-modelling, in a related study, applying the results from their arterial tree model (Walrand et al. 2014b).

Debbaut et al. (Debbaut et al. 2014) demonstrated, by corrosion casting and micro-CT imaging, that the native hepatic artery tree deviates much from an idealised dichotomous bifurcation model, in which a parent artery is divided

into two daughter arteries; the latter is therefore an overly simplified version of a native hepatic artery tree. It is of interest to identify the volume for which a dichotomous bifurcation model can accurately simulate microsphere deposits and to determine whether such a volume is dependent on microsphere concentration. Clinical gains are expected from validation/modification of the mentioned branching artery tree model, by Walrand et al, with findings of microsphere distributions in dissected NL tissue and, if necessary, inclusion of more parameters in a similar model, with the possibility to obtain more realistic small-scale as well as macroscopic absorbed dose distributions. One clinical gain of a more accurate microsphere and absorbed dose distribution model is a subsequently better explanation of tolerance and risk of toxicity. Optimisation of number of injected spheres (and/or modification of activity per sphere) or variation of other parameters, such as sphere diameter, radionuclide, etc., may also become feasible. The construction of such a modified arterial tree model is another important objective of this thesis.

1.7 Radiation safety and surgery

The absorbed dose rate to the hands, for the technologist (at preparation) and the physician (at administration) is about $0.7 - 1.0 \text{ mSv h}^{-1}$ (SIRTeX, 2007). Each exposure time is, typically, about half an hour, hence not causing any serious issues concerning radiation safety.

Surgery on highly radioactive patients is, however, not a common procedure; special caution and awareness are therefore needed. Even though only about 10% of the radioactivity is left at time of surgery (after 9 days of post-therapeutic physical decay), it can be expected that the exposure of the surgeons hands will be much higher, than for the personnel involved in RE administration. There are two main reasons for this, i) direct finger- and palm contact (albeit gloves are used) with the radioactive (both tumour and NL) tissue and ii) a several times longer exposure time. The absorbed dose limit for the extremities and body skin of radiation workers is 500 mSv yr^{-1} (Directive 1996). It is crucial to estimate how many (if any) complete surgical procedures that can be performed, without the surgeon transcending the annual limit. Such estimations are possible with computer simulations and could be evaluated with measurements on resected tissue; both methods are accounted for in this work.

“If you do not know where you are going, any road will get you there”

-Lewis Carroll

2 AIMS

The aims of this thesis can be divided into two main categories.

2.1 Microsphere and absorbed dose distribution characteristics

Aims regarding distribution parameters were focused on NL tissue.

1. To describe macroscopic heterogeneity in the distribution of microspheres on a therapeutically relevant geometric scale considering the range of ^{90}Y β -particles
2. To study small-scale heterogeneity by the occurrence and size of microsphere clusters in relation to biopsy MAD and simulate small-scale absorbed dose distributions based on mentioned biopsy sphere-cluster distributions
3. To create a hepatic artery tree model, able to reproduce NL microsphere distributions and predict absorbed dose distributions

2.2 Radiation safety during surgery

To develop and evaluate a method of predicting absorbed dose rate to the surgeon's hands during liver resection on still radioactive RE patients, through computer simulations and TLD measurements on resected tumour and NL tissue

“If I had eight hours to chop down a tree, I would spend six hours sharpening my axe”

-Abraham Lincoln

3 PATIENTS AND METHODS

3.1 Patients (I,II,III,IV)

Two female patients, age 33 (Pt 1) and 62 (Pt 2) years suffered cholangiocarcinoma, confined to the liver, but only marginally resectable, because of proximity to critical vascular and biliary structures. Both patients were selected for neo-adjuvant treatment, with RE, followed by marginal resection, aiming for reduced risk of local recurrence at resection margins. Pre-study CT investigations revealed that Pt 1 had tumour masses of 770 (left lobe) and 180 g (right lobe), with NL tissue of 100 and 1200 g in respective lobes; Pt 2 had tumour masses of 37 (left lobe) and 56 g (right lobe), close to vena cava, liver veins and PT, with NL of 700 and 1350 g, respectively.

3.1.1 Pre-therapeutic investigations

Before RE treatment, the vascular properties of tumour regions were examined, in order to assure safe treatment; the patients were investigated by selective hepatic artery angiography and artery coiling, followed by infusion of ^{99m}Tc -MAA. Information about expected therapeutic tumour and NL distribution, TNC and the risk for excessive pulmonary shunting could be obtained, by planar imaging and SPECT/CT with a GE Millenium VG camera (energy window 126-154 keV), with high resolution (HR) collimator. The image matrix was 256×256 , with voxel size 2.21 mm, resulting in a field of view (FOV) of $57 \times 57 \text{ cm}^2$. The iterative ordered subset expectation maximisation (OSEM) algorithm was used for tomography reconstructions.

3.1.2 Radioembolisation

For both patients, the hepatic artery was recannulated for infusion with SIR-Spheres, two weeks after ^{99m}Tc -MAA examinations. Table 2 shows the administrated activities and number of spheres injected during less than an hour, suspended in 30-40 ml of distilled water. The remaining activity concentrations, at the respective days of surgery, are also shown in the table. The large-scale distribution of administrated activity was examined by bremsstrahlung detection, with the same imaging method and parameters, but with another energy window (55-285 keV) and a medium energy (ME) collimator. The comparison of ^{90}Y bremsstrahlung and pre-therapeutic ^{99m}Tc images revealed some large-scale deviations, larger for Pt 1, but with no signs of administration failure, such as excessive shunting, for any of the patients.

Table 2. Injected activities and approximate number of spheres at RE and activity concentrations at surgery (9 days post-RE). T means tumour and NL normal liver tissue. When numerical values are absent, knowledge of actual values is missing.

	Patient 1			Patient 2			
	Left lobe	Right lobe		Left lobe		Right lobe	
	T	NL	T	NL	T	NL	T
Activity (GBq)	1.5	-	0.90	-	1.0	-	0.56
Number of spheres	30×10^6	-	18×10^6	-	20×10^6	-	12×10^6
Activity conc. (kBq cm ⁻³)	190	50	140	65	250	64	250

3.1.3 Surgery

On the ninth day post-RE, the patients were re-admitted for surgery. The objective of the resection procedure was removal of macroscopic tumour, including a substantial rim of surrounding NL tissue, when possible. Dissection was performed with an ultrasonic cavitron aspirator. The resected tissue was immediately immersed in isotonic formaldehyde for 48 hours.

3.2 Surgery radiation exposure (I)

3.2.1 Simulations

Simulations of dose rate to fingers from β -radiation were performed with the software VARSKIN[®] Mod 2 (J S Durham, Pacific Northwest Laboratory, USA). The VARSKIN code is based on a beta dose point kernel algorithm, averaged over an area of 1 cm². The reliability of the code has been tested by independent users and has shown good agreement with Monte Carlo simulations (Sherbini et al. 2008), performed with the MCNP code for β endpoint energies from 0.3 to 2.3 MeV, thereby including 2.28 MeV, the endpoint energy of ⁹⁰Y. The mean yield and fraction of absorbed dose from bremsstrahlung, as compared to electrons, were expected to be as low as 0.3-0.4% and 0.1-0.2% (Stabin et al. 1994), respectively, and the bremsstrahlung

absorbed dose was therefore neglected. Technical details about the simulation procedure can be found in Paper I.

3.2.2 Measurements on resected tissue surface

Some resected tissue volumes were foiled with 0.4 mm transparent plastic, with similar shielding properties as polystyrene plastic, specified in the simulations. Thermoluminescent dosimeters (TLD), with a size of $3 \times 3 \times 1$ mm³, were taped with square side facing the outside of the foil, which was covering the tissue. For Pt 1, 10 TLDs were taped on the shortest side of a slice with a 1×2 cm² cross-section area (See Paper I), containing tumour and NL tissue; for Pt 2, 15 TLDs were taped on tissue shaped as a spherical cap (See Paper I). The corresponding absorbed dose rates on tissue surface in the middle of surgery, representing the average absorbed dose rate during surgery, was calculated by decay correction (See Paper I).

3.3 Radioactivity in resected tissue (II, III)

3.3.1 Activity and microsphere detection

Some resected tissue, from both patients, was machine sliced into sections, approximately 1 to 8 mm thick for Pt 1 and 1 to 2 mm thick for Pt 2.

Autoradiography

Every other slice was covered in double layers of 0.2-mm plastic film and exposed to autoradiography films (Amersham Hyperfilm[®] MP, GE Healthcare, Uppsala, Sweden) in cassettes (Pt 1: for 5 h, 5 days after surgery; Pt 2: for 2 h, 3 days after surgery).

Gamma well counter measurements

The remaining slices were punched into various sizes (diameters 3, 4, 6 and 8 mm), with masses 8 to 422 mg for Pt 1 and 5 to 102 mg for Pt 2. Each punch biopsy was weighed and immersed in 1 ml formaldehyde (10 %), in plastic vials with an inner diameter of 9 mm and a wall thickness of 1 mm. The biopsy-specific activity was measured from bremsstrahlung, in an automatic gamma well counter (Wizard[®] 1480, PerkinElmer, Waltham, MA, USA), calibrated for known ⁹⁰Y activity, with a relevant activity interval, in the same vial type and formaldehyde (10%) volume. The activity concentration at day of injection (and absorbed dose, assuming complete decay from day of injection) was calculated by decay correction (See Paper I for equation).

Microscopy

A smaller sample, 6 punch biopsies (4 to 8 mm diameter) of NL from Pt 2, was sectioned, (10 serial sections per biopsy), 20 μm thick (Paper II). Another 16 NL punch biopsies was selected from Pt 2, for a more rigorous analysis of microsphere distributions, related to activity concentration. The punch biopsies of the larger sample were chosen, aiming for intra-sample mass homogeneity (6 to 8 mm diameter) and activity concentration heterogeneity (Paper III). The orientation of the sectioning was optimized for cluster tracking (transversal to vessels). Each biopsy was sectioned in 15 sections, with thickness 30 μm . All biopsies were paraffin embedded before sectioning and stained with haematoxylin-eosin (Campbell et al. 2000).

3.3.2 Analysis of tissue activity heterogeneity

Macroscopic distribution

Autoradiography was performed in order to obtain an overview of two-dimensional pattern tendencies and degree of heterogeneity, which could be of complementary use in analysis of biopsy measurements with gamma well counter. As mapping of the exact locations of activity units (i.e. microspheres) over a large volume is very tedious, it was not feasible to perform rigorous spatial distribution statistics, e.g. by applying Ripley's K function, describing cluster formation tendencies by measurements of average distance between signal points in relation to expected distance in a randomised Poisson (i.e. homogeneous) distribution, the latter not influenced by structural variations (Kiskowski, Hancock and Kenworthy 2009). The relative heterogeneity of the microsphere distribution was instead calculated in a straightforward way, by the coefficient of variation (CV) and the skewness (SK), by the adjusted Fisher-Pearson standardised moment coefficient (Doane and Seward 2013) (See Paper II for details).

The intuitive approach was that a rapid decrease of CV and SK with increasing element size (biopsy mass), within mass-specific samples, would indicate a heterogeneous pattern larger than the element size, i.e. individual biopsy volumes (Pickett and Cadenasso 1995, Wu 2004, Lam and Quattrochi 1992, King, Johnson and O'Neill 1991). A heterogeneous pattern, with a basic unit (patch) larger than the mean range of the β -radiation, would not be homogenised by crossfire effects. A heterogeneous pattern with a basic unit of the same size as the smallest mass group or smaller is expected to show little mass dependence for CV and SK and the variance found within all samples would probably be explained by a combination of stochastic effects and expected presence of systematic variance, i.e. tissue absorbed dose gradients on a much larger, detectable with external imaging methods. As different sized punch biopsies are collected in a similar geometrical fashion,

the suggested method is expected to reveal heterogeneous patterns on a moderate scale, also within a distribution that is affected by larger dose gradients and by stochastic variance, expected to cause similar variation within all samples.

To strengthen the argument for this approach, the effect is demonstrated on the heterogeneous, but repetitive, idealised, non-randomised pattern, shown in Figure 2. The symbols [\cdot], [$+$] and [$*$] represent signal values 1, 4 and 16, respectively. The pattern size is 3×6 or 6×3 , which means that if the signal is averaged within area elements of exactly size 3×6 (independent of orientation) or 6×6 , there would be no variation (i.e. mean signal = 2.1; CV = 0 and SK = undefinable). Even in the most consistently repetitive pattern, from a real sample, there will always be some stochastic variation (noise), but in this example, only the idealised pattern is considered. For small elements, high CV and SK are expected, rapidly decreasing with element size.

In the nine samples described by the plots in Figure 3, each sample contains output from 64 equally-sized area elements (Figure 2B). The sampling is done, stepwise, (overlapping for sizes > 1) by letting each element cover an element-unique geometric space. This procedure is similar to down-sampling (Loew et al. 1980) an image with the nine shown different element areas used as masks. In the present example, overlapping of previous elements is allowed, in order to collect large enough samples from the limited pattern area of 10×10 square units.

The first sample would therefore cover a total pattern area of 64 squares, the second 72, the third 80 etc., up to the entire pattern of 100 squares for the last sample, with elements 3×3 squares wide. As the total area investigated is considerably larger than the repetitive pattern, for all element sizes, and the samples are fairly large, the output is not expected to suffer from severe edge effects, or low representativeness, as compared to randomised spatial sampling within a larger area of the same repetitive pattern.

Although the output values of signal averaging (not shown) are highly discretised, as a consequence of the lack of randomisation in the pattern, the trends for the distribution parameters are clear: both CV and SK decrease rapidly for small elements; the decrease is still present, but less dramatic, for larger elements.

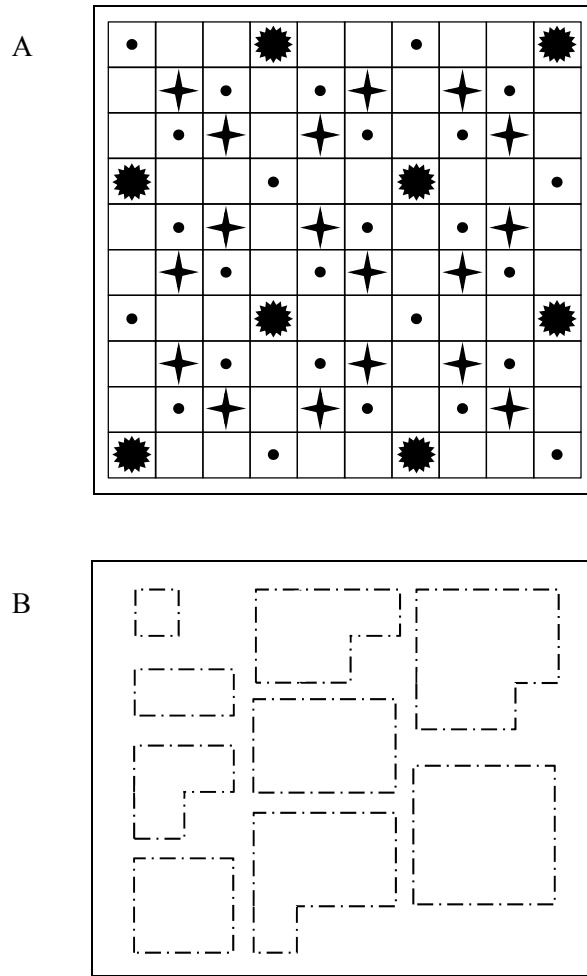


Figure 2. A signal pattern is shown in (A); the signal values of 1, 4 and 16 are illustrated with the symbols [·], [✦] and [☀], respectively. The repetitive pattern has the size 3×6 or 6×3 area units. Nine samples are gathered, containing 64 signal-averaging elements per sample; each sample contains equally sized sample-unique area elements, one of the nine different area elements shown in (B). The 64 sample elements are uniquely distributed, with edges aligning the 10×10 square grid, but the separate elements within a sample are allowed to overlap geometrically; the entire samples cover 64 to 100 of the 100 squares in the pattern, with larger coverage for samples with larger element area size.

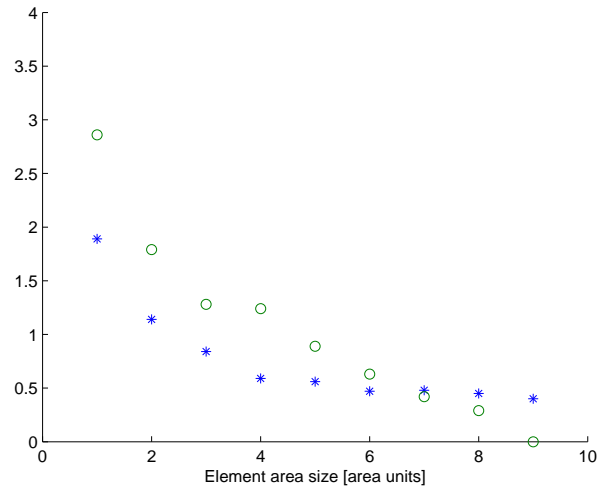


Figure 3. The plots show the distribution parameters for the samples described in Figure 2, specified for the element-size unique samples. The average of all samples, for their intrinsic mean signal per element (data not shown), is 2.04 ± 0.03 . Both CV [o] and SK [*] decrease non-linearly with element size; the decrease is more dramatic for smaller element sizes.

Small-scale distribution

The sections were investigated sequentially for single and aggregated microspheres, in order to track clusters distributed within the same artery/arteriole, through more than one section; a cluster was defined as two or more spheres with an approximate inter-sphere distance of 0.2 mm (i.e. no more than 8 sphere diameters) or less. The clusters were found as thin strings of single spheres or wider sphere conglomerates, either densely or sparsely packed (with one or more cross-sections of the same cluster lacking spheres). Due to chosen orientation, most clusters were sectioned trans-axially, but some clusters were distributed in a more diagonal fashion throughout the sections.

3.3.3 Simulation of absorbed dose (III)

Simulations of small-scale absorbed dose distribution were performed, based on the microsphere distributions found in the 16 microscopically scrutinised punch biopsies, mentioned in section 3.3.1 (the smaller sample of 6 punch biopsies, studied with the simplified method, was not included). The simulations were performed by i) spatial randomization of activity loci from the microscopically registered sphere distribution, containing single spheres and clusters, up to the activity measured sphere concentration (MAD, assuming CPE), ii) convolution of mentioned, semi-randomised, virtual activity volumes with a ^{90}Y beta dose point kernel, according to Prestwich et al (Prestwich, Nunes and Kwok 1989), tuning the absorbed fractions for centremost voxels, according to Siegel and Stabin (Siegel and Stabin 1994) and iii) obtaining absorbed dose distributions, based on the sub-volume of each output matrix where the conditions for charged particle equilibrium (CPE) was fulfilled. A consequence of this was that MAD became directly coupled with activity concentration. The simulation process (i.e. technicalities) is described in further detail in Paper III.

3.3.4 Statistics

Median, mean \pm standard deviation (mean \pm SD), CV and SK were used to describe normally distributed continuous variables. Relationships were evaluated by linear regression, applying Ordinary Least Squares (OLS), to either the dependent variable data point set or its logarithmised data point set. Hypothesis tests (two-sided t -test) were performed, $\alpha = 0.05$.

3.4 Simulation of arterial tree model (IV)

3.4.1 Microsphere distribution

Microsphere distributions, with different MADs as end points, were used in an adapted version of the branching artery tree model described by Walrand et al (Walrand et al. 2014a) (See section 1.6). The adaption was made by introducing variability in the microsphere and artery diameters. The mean artery diameters were exponentially decreasing. Three variable parameters were optimised to obtain concordance between simulations and microsphere distributions: a combined artery coefficient of variation (ACV) parameter for the inner diameter of all artery generations throughout the virtual tree structure and the microsphere flow distribution at the nodes, the hepatic tree distribution volume (HDV) parameter, and the embolisation (EMB) parameter, that reduces the artery diameters. The model was tested against the measured sphere distribution in 16 biopsies with microsphere

concentrations of 14 spheres per mg, and also when these biopsies was divided into three groups with different mean microsphere concentrations: 4.6 (n=5), 13 (n=6), and 28 (n=5) spheres per mg tissue. The CV of the microsphere diameters was set to 0.077, in accordance with reported distributions ($32.5 \pm 2.5 \mu\text{m}$), (mean \pm SD), for SIR-Spheres (Nelson et al. 2008, Cremonesi et al. 2014) (See section 1.3.2).

3.4.2 Absorbed dose distributions

The simulations of absorbed dose distributions were performed in a similar way, as described in section 3.3.3 (See Paper IV for technical details). The accumulation of spheres in different generations of the branching artery tree was divided into sub-volumes, but the exact position of the spheres within the sub-volumes were geometrically randomised, as the native arterial tree is structured and organised, but with much variation in size and shape of the liver lobules and, therefore, the locations of individual PTs (Debbaut et al. 2014, Rappaport et al. 1954, Saxena, Theise and Crawford 1999), which is demonstrated in Figure 4.

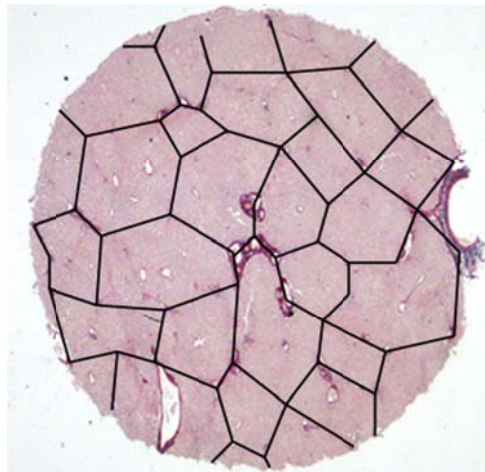


Figure 4. Both size and shape of the liver lobules are found to vary considerably, as compared to the idealised view of a more homogeneous structure of idealized hexagonal lobules of equal size. The diameter of the shown biopsy is about 8 mm, implying the shown lobule diameters to vary from less than 1 mm up to more than 2 mm, in agreement with previous studies (Crawford et al. 1998, Debbaut et al. 2014).

“We don't see things as they are, we see them as we are”

-Anaïs Nin

4 RESULTS

4.1 Pre-therapeutic imaging (I,II,III,IV)

The planar imaging revealed low pulmonary shunting fractions of 3.0% (Pt 1) and 3.5% (Pt 2), and averaging voxel signal in the entire tumour and NL tissues by SPECT/CT, showed sufficiently high TNCs of 2.7 (Pt 1) and 3.8. Assuming complete in-vivo decay when performing calculations (i.e. without surgery) the prescribed activities (see section 3.1.2) were expected to result in the following total liver MADs: Pt 1: tumour: 59 Gy, NL: 22 Gy; Pt 2: tumour: 125 Gy, NL: 33 Gy. Due to resection, 9 days post-RE administration, the resected tissue would receive 90% of the above in-vivo absorbed dose.

4.2 Surgery radiation exposure (I)

Results of both simulations and measurements of absorbed dose rate to tumour tissue, including different number of glove layers (simulations) and with the actual radiation protection layer for TLD measurements are shown in Table 3. Considering TNCs of 2.7 and 3.8 (see section 4.1), the corresponding absorbed dose rate on NL tissue is expected to be, typically, < 40% of mean absorbed dose rate on tumour tissue.

4.3 Radioactivity in resected tissue (II,III)

4.3.1 Autoradiography (II)

Autoradiograms of resected tumour and NL tissue are shown in Figure 5. The patterns reveal a generally higher activity concentration in tumour than in NL. The patterns are inhomogeneous, with both aggregated areas (hot spots) and areas with limited activity concentration (cold spots).

Table 3. Simulations and measurements of decay-corrected absorbed dose rate levels on tumour tissue of Pt 1 and Pt 2, including radiation protection with gloves. Absorbed dose rate measurements on tumour tissue with TLDs are shown in the two rightmost columns; for Pt 1 a sample of 8 elements (TLD positions) and 15 elements for Pt 2. Each glove layer was simulated as 0.2 mm polystyrene plastic.

Glove layers	Simulations (mSv h ⁻¹)		Measurements Mean ± SD Max (mSv h ⁻¹)	
	Pt 1	Pt 2	Pt 1	Pt 2
0	53	65		
2	39	47	45±24 81	45±22 87
3	32	40		
4	27	36		

4.3.2 NL tissue activity distributions

Biopsies were gathered for both NL and tumour tissue. The total available number of tumour biopsies within narrow mass intervals was low (totally 25 for Pt 1 and 41 for Pt 2, both samples with a wide mass range). As the main focus of this work is on NL tissue, the data shown here are from NL tissue only (For comparison with tumour data, see details in Paper II). For Pt 2, much NL tissue was available and substantial gathering of biopsies was feasible, as shown in Figure 5. The total number of NL punch biopsies from Pt 1 was 96 and the corresponding number from Pt 2 was 159. In Tables 4 and 5, the distribution parameters for NL tissue from Pt 2 are shown (Table 4, adjacent to tumour; Table 5, far away from tumour). The distributions presented in Table 5 are also presented in distribution histograms in Figure 6, thereby facilitating the interpretation of the distribution parameters CV and SK, for the actual case. The decreasing CV and SK with increasing activity concentration is apparent in both Tables 4 and 5, as well as in Figure 6.

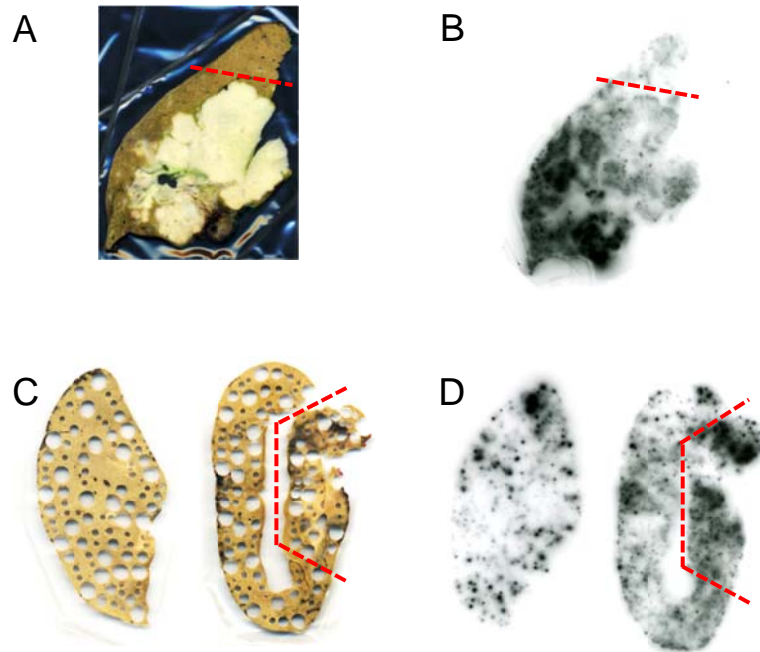


Figure 5. Photographs (A and C) and corresponding autoradiograms (B and D) of tissue from Pt 1 and Pt 2; for Pt 1 (A and B), there are only small regions of normal liver tissue, outlined at the top of the images, the rest being tumour. For Pt 2 (C and D), the normal tissue was dominant in the investigated sample; the only part of the two separate sub-volumes being tumour is outlined at the rightmost ends of the panels. The punch samples, explaining the perforation of the tissue (C), were collected after autoradiography.

Table 4. Activity distributions in NL tissue adjacent to tumour of Pt 2; CV represents the coefficient of variation, \bar{m} the mean mass of n tissue biopsies, Spheres/biopsy, the average number of spheres per biopsy, A/m the mean activity concentration and SK the skewness of the distribution

Mass (mg)	Small $5 \leq m \leq 14$	Medium $16 \leq m \leq 41$	Large $43 \leq m \leq 102$	All $5 \leq m \leq 102$
\bar{m} (mg)	10	27	69	35
n	26	24	25	75
Spheres/biopsy	380	920	2300	1200
A/m (Bq/mg)	1900	1700	1700	1700
CV	0.81	0.58	0.45	0.64
SK	1.8	1.2	0.69	1.9

Table 5. Activity distributions in NL tissue far away from tumour of Pt 2; CV represents the coefficient of variation, \bar{m} the mean mass of n tissue biopsies, Spheres/biopsy the average number of spheres per biopsy, A/m the mean activity concentration and SK the skewness of the distribution

Mass (mg)	Small $6 \leq m \leq 14$	Medium $15 \leq m \leq 39$	Large $40 \leq m \leq 91$	All $6 \leq m \leq 91$
\bar{m} (mg)	10	27	66	35
n	29	26	29	84
Spheres/biopsy	300	590	1200	740
A/m (Bq/mg)	1500	1100	900	1040
CV	1.4	1.0	0.63	1.3
SK	3.0	1.8	0.82	4.0

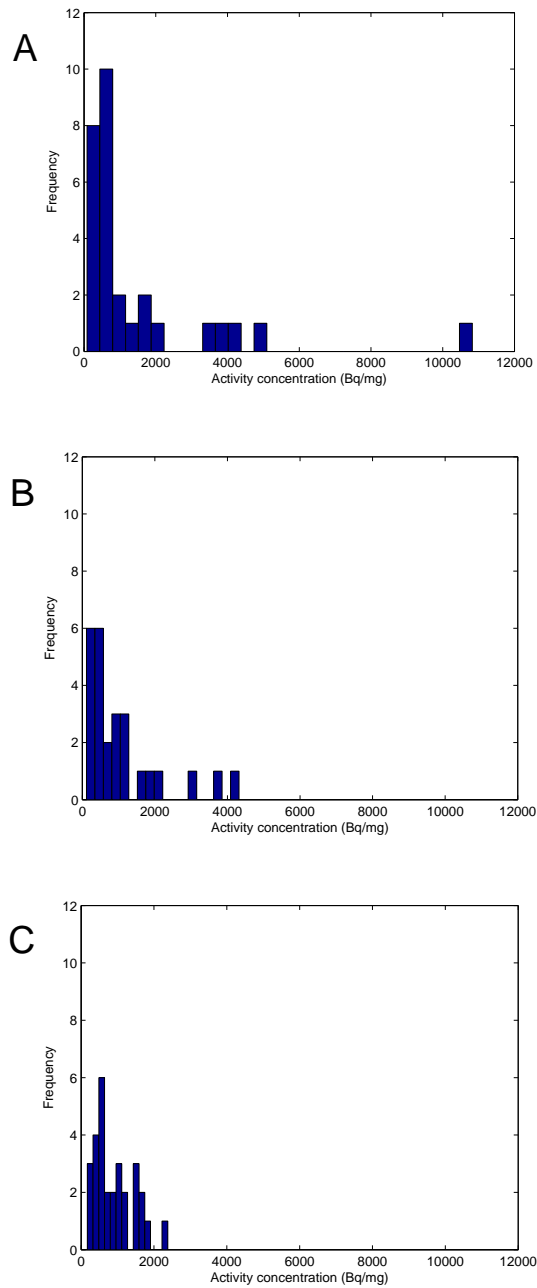


Figure 6. The CV of the activity concentration distribution is shrinking with increasing biopsy mass, within NL of Pt 2; (A) masses 6 to 14 mg, (B) masses 15 to 39 mg and (C) masses 40 to 91 mg. All distributions are divided into 11 bars; note that this implies different bar widths.

4.3.3 NL tissue microsphere distributions

The investigation of the smaller NL tissue sample of 60 sections, from six punch biopsies of Pt 2, revealed 240 locations with a total of 793 microspheres; 154 (64%) of the locations were single spheres, representing only 19% of all spheres. 53% of all spheres were located within any of the 19 largest clusters (7% of the locations), ranging from 8 to 59 spheres per cluster (see Paper II for detailed information). The investigation of the larger NL tissue sample of 240 sections, from 16 punch biopsies of Pt 2, revealed 3888 spheres (152 single spheres and the remaining 3736 spheres in clusters of different size). The 3736 aggregated spheres were found within 277 clusters, many of them distributed throughout several sections and some throughout all 15 available biopsy-specific sections. Assuming CPE, the combined well counter- and scales-measured activity concentrations did correspond to the following MADs for the 16 biopsies: 8, 12, 17, 19, 21, 24, 29, 33, 38, 46, 48, 54, 56, 59, 61 and 84 Gy. Clusters with different number of spheres per section are shown in Figure 7. Figure 8A shows the distribution of cluster sizes and Figure 8B illustrates the strong correlation between cluster size and number of spheres per section (i.e. larger clusters are found in PT arterioles/arteries with larger diameters). Figure 9 demonstrates the exponentially increasing maximum cluster size with increasing MAD. A general trend of increasing proportion of microspheres in increasingly larger clusters with increasing MAD was also apparent (See Paper III).

Simulated absorbed dose distributions (III)

Figure 10 shows how CV of the small-scale absorbed dose distribution increases linearly with increasing MAD.

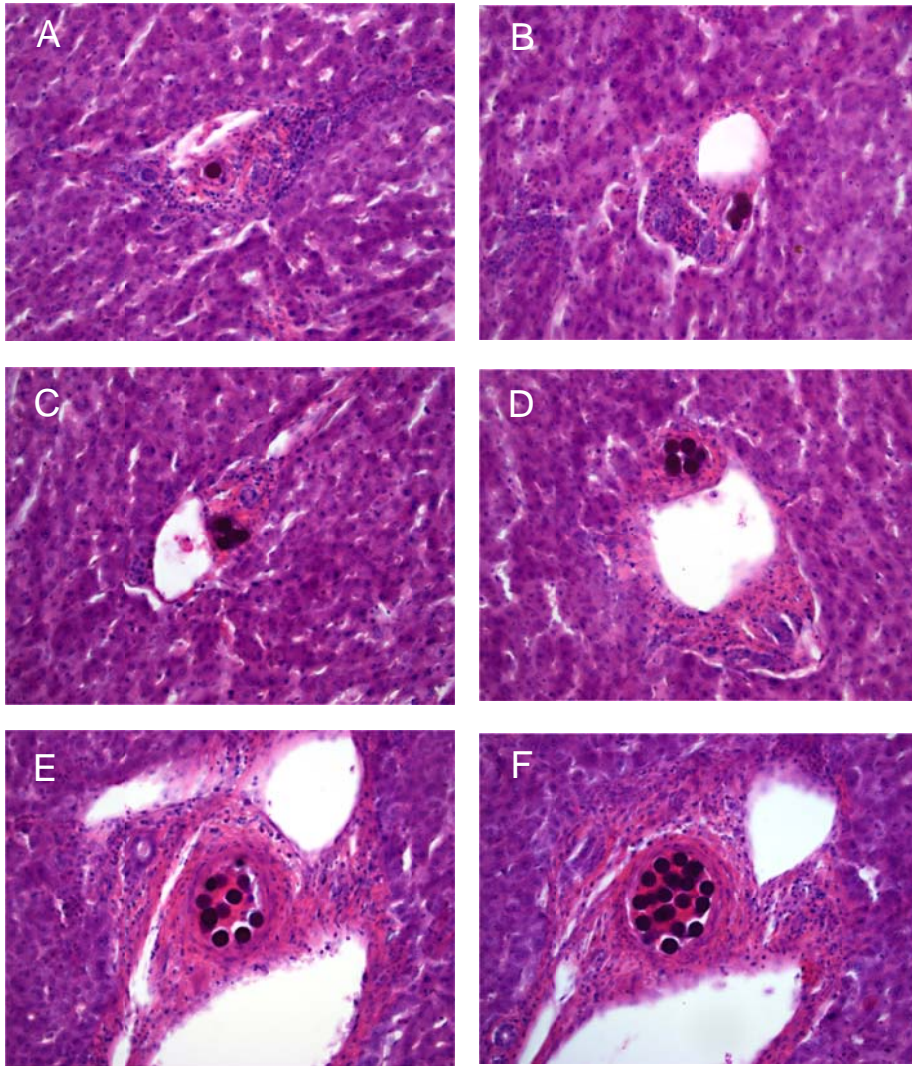


Figure 7. The images show the versatility of number of spheres per cross-section, strongly correlated with cluster size, from single spheres (A), 2 to 10 spheres per cross-section (B – D), up to over 10 spheres per cross-section; (E) and (F) illustrate how the same cluster, in some cases, decreases in cross-section size throughout the 15 subsequent sections. Compare with Figure 8B

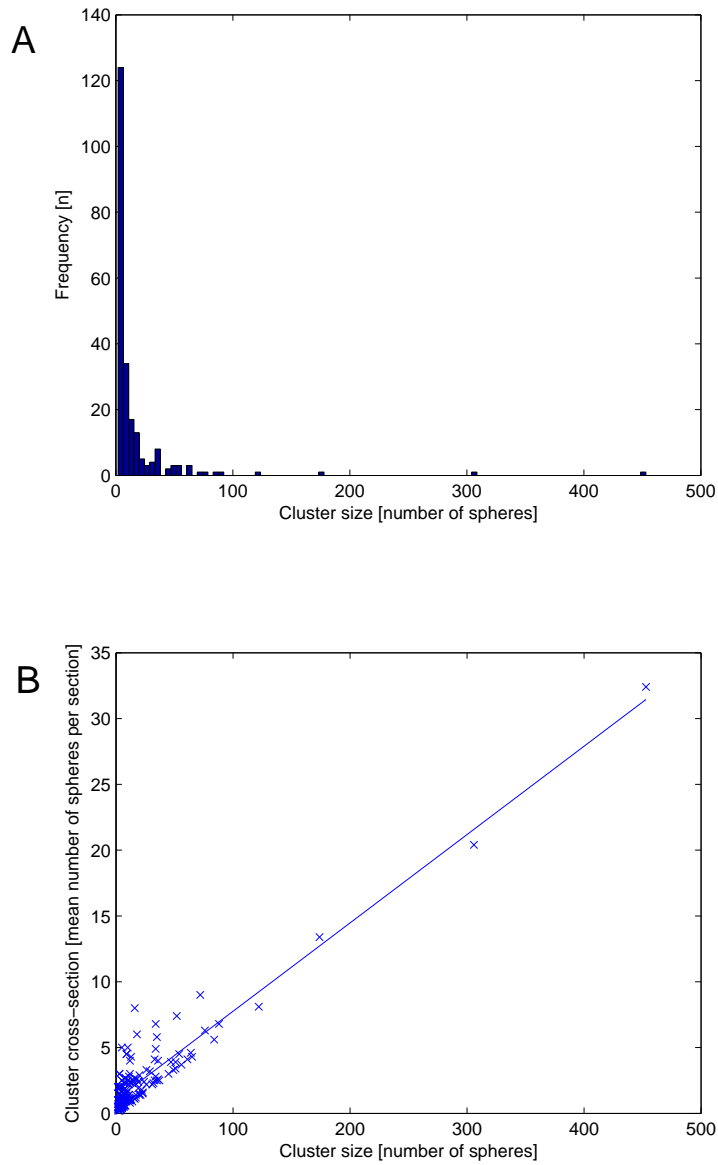


Figure 8. (A) Histogram of cluster size and frequency. Clusters > 100 spheres per cluster are rare, but each of these clusters houses a large fraction of the total number of spheres; (B) The cross-section size is found to increase linearly with cluster sizes, especially for larger clusters, reflecting the tendency of finding larger clusters in larger arterioles/arteries.

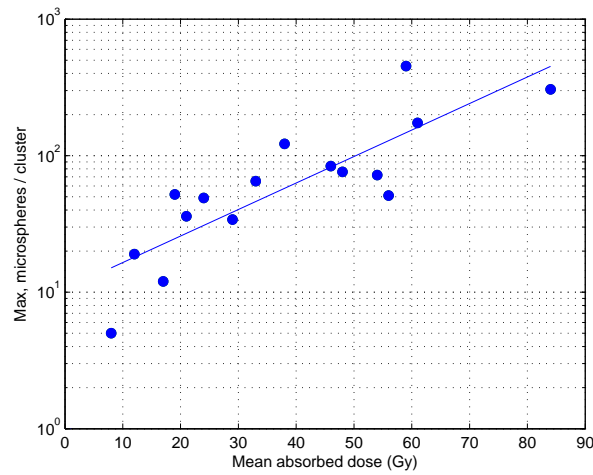


Figure 9. The largest cluster size in each of the 16 biopsies and the corresponding trend line for exponential increase, from approximately 16 spheres per cluster at 10 Gy to 400 spheres per cluster at 80 Gy. The cluster size levels increase exponentially with the mean absorbed dose in the biopsies.

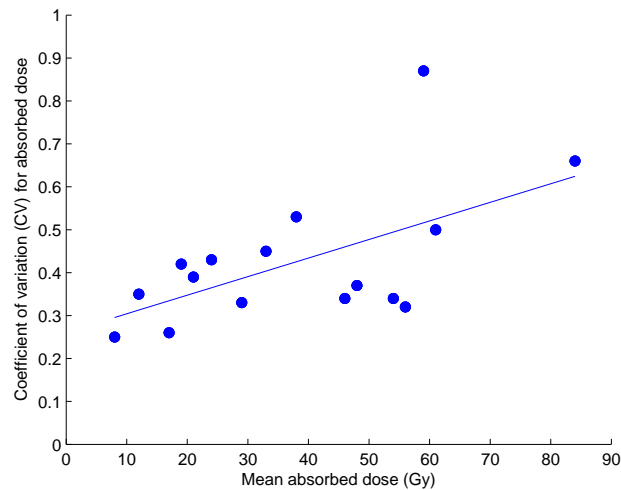


Figure 10. The CV of small-scale absorbed dose increasing with mean absorbed dose; the 16 separate absorbed dose simulations were based on cluster distribution patterns of the microscopic sub-samples, but added up to the mean absorbed dose within the specific biopsy, the mean absorbed dose based on activity measurements with gamma well chamber, assuming charged particle equilibrium. The resulting graph shows a linear increase in CV of the absorbed dose, with biopsy mean absorbed dose.

4.4 Arterial tree simulations (IV)

4.4.1 Microsphere distribution

Figure 11A shows the distributions from the 16 biopsies, with high frequency for small clusters but the low frequency regions contain several hundreds of spheres per cluster. The cluster deposits are mainly found within higher artery generations (Figure 11B) and less frequently within larger arteries (lower generations). However, the largest clusters were always located in the largest arteries.

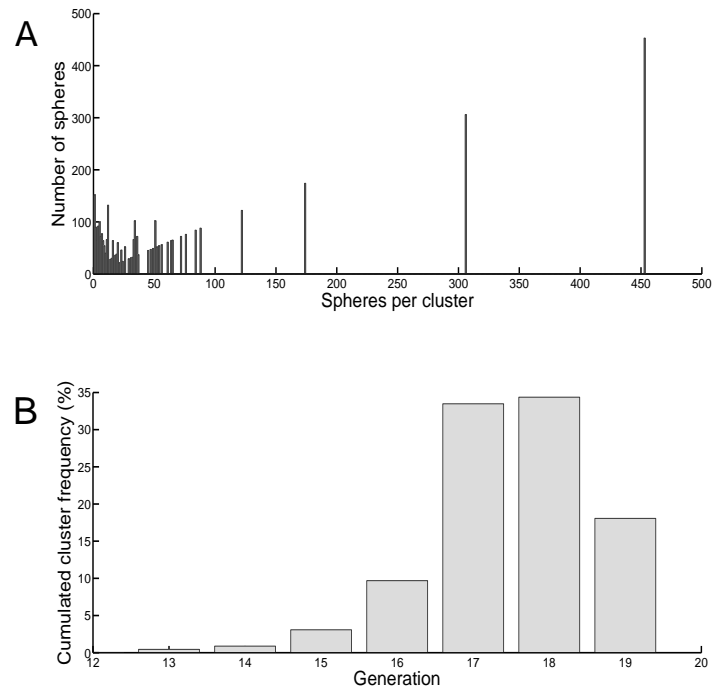


Figure 11. The distribution of the spheres in 16 biopsies, with a mean concentration of 14 spheres/mg. A) The distribution of number of spheres vs. spheres per cluster. B) The distribution of sphere clusters in the different artery generations. The spheres were found in artery and arteriole diameters that correspond to the artery generations 13 to 19. Microspheres which were considered to be located in arteries and arterioles with diameters less than the microspheres were collectively placed in the 19th generation. This was performed due to difficulties to accurately determine the inner diameter of small vessels.

For the parameter values: $ACV=0.35$, $HDV=50\text{ cm}^3$ and $EMB=6\text{ }\mu\text{m}$, harmony was found between simulated and measured cumulative frequency of the microsphere distribution versus both spheres per cluster and artery generation for the 16 biopsies ($R^2>0.99$) (Figure 12A-B). These parameter values also generated similar agreement between simulated and measured CV for different sized samples.

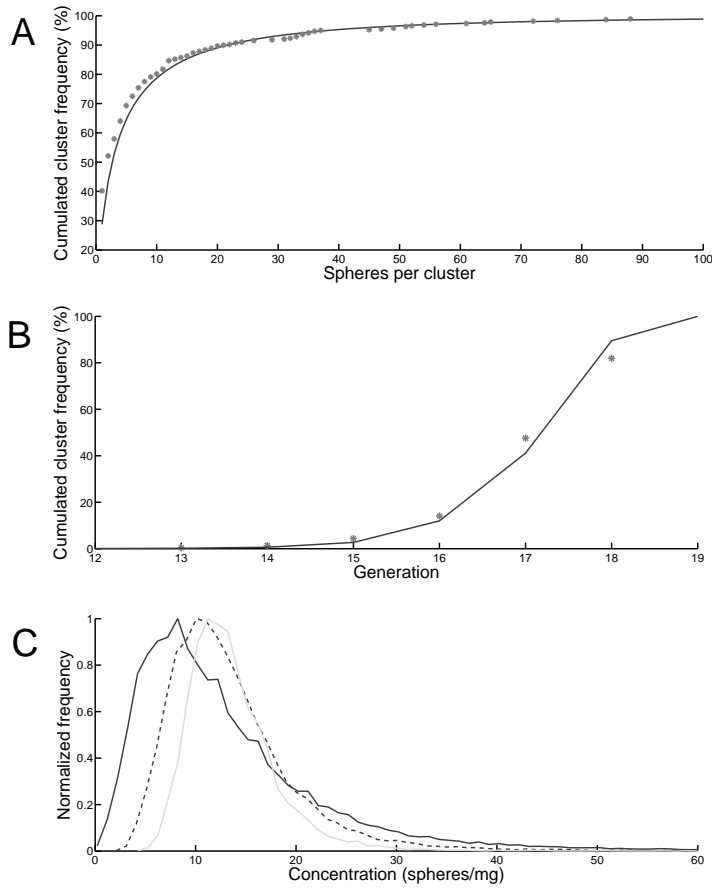
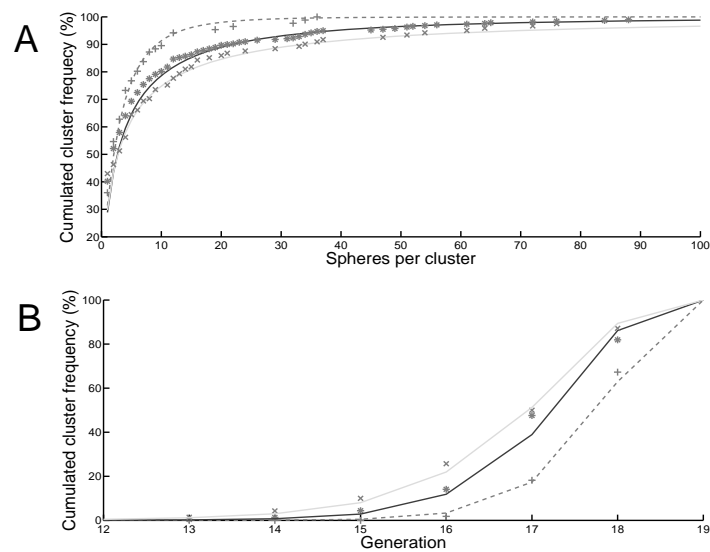


Figure 12. Comparison of simulations and measured sphere distributions for sphere concentration of 14 spheres/mg. A) The cumulative cluster frequency vs. spheres per cluster, and B) the cumulative cluster frequency vs. artery generation, for the measured biopsies [*] and simulation (line) ($r^2>0.99$). C) Simulation of the sphere concentration distribution in 10 (black line), 27 (black dotted line) and 66 mg (grey line) samples revealed more normally distributed frequency curves and decreasing CV for higher microsphere concentrations.

Figure 12C shows the simulated sphere distribution for three sample sizes; the CV for the 10, 27 and 66 mg samples is 1.4, 1.0 and 0.56, respectively. Corresponding CV for the punch biopsy measurements was 1.4, 1.0 and 0.63, respectively (See Table 5).

Figure 13 shows the cumulative frequency of the microspheres distribution for the three microspheres-concentrations and the concordance with the best fit to the simulations ($R^2 > 0.98$). In comparison to the mean sphere concentration (14 spheres mg^{-1}) ACV and EMB decreased to 0.20 and 2 μm , respectively, for lower sphere concentration (4.6 spheres mg^{-1}) and HDV increased to 130 cm^3 . For higher sphere concentration (28 spheres mg^{-1}) the opposite was obtained; the optimal parameter values were then: ACV 0.46, HDV 22 cm^3 and EMB 8 μm .



The cumulative cluster frequency versus A) spheres per cluster and B) artery generation for the measured biopsies*[,+,*,x] and simulation [line]. Simulation of sphere distribution for the different sphere concentrations resulted in different parameter values. The best fit to the mean biopsy sphere concentrations of 4.6 (+ and dotted line), 14 (* and black line), and 28 (x and grey line) spheres/mg was obtained for: ACV of 0.26, 0.35, and 0.46, respectively; HDV of 130, 50 and 22 cm^3 , respectively; EMB of 0, 6 and 8 μm , respectively; ($r^2 > 0.98$).

4.4.2 Absorbed dose distributions

Figure 14 shows the absorbed dose distribution for three microsphere concentrations, corresponding to MADs of 9, 35 and 65 Gy, respectively. Figure 14D-F shows how the section-averaged absorbed dose variation increases with increasing MAD. The CV is 0.19, 0.41 and 0.57 for the MADs of 9, 35 and 65 Gy, respectively. The corresponding interpolated CV based on dosimetry on NL tissue biopsies was 0.30, 0.41, and 0.54, respectively (See Figure 10).

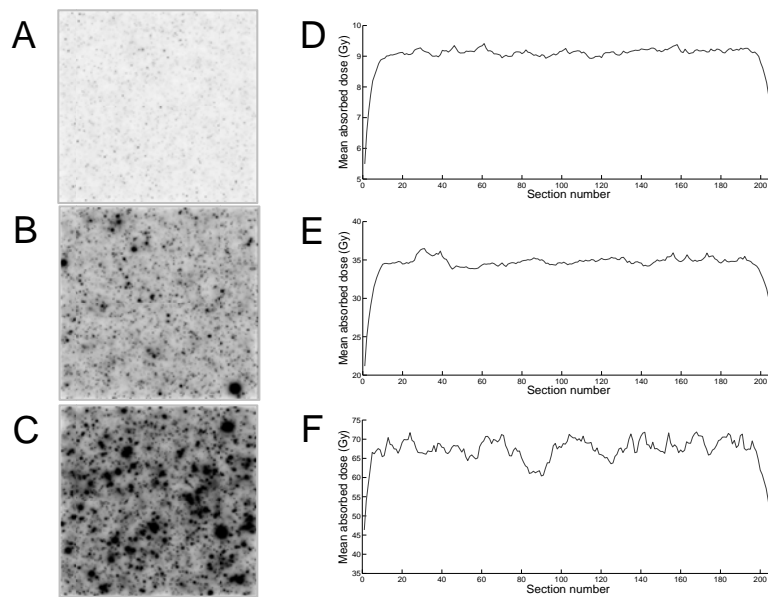


Figure 13. The simulated absorbed dose distribution in liver tissue for mean concentrations of 4.6, 14 and 28 spheres/mg. (A-C) shows the voxel absorbed dose distribution in three cross sections of 80 cm^2 , with MADs of 9.0, 34 and 65 Gy, respectively. The greyscale indicates the absorbed dose, where the values are truncated at 100 Gy (100 Gy = black) for improved visualisation. (D-F) shows MAD in different 80 cm^2 cross sections throughout the simulated liver volume, totally 207 sections.

“Clear thinking requires courage rather than intelligence”

-Thomas Szasz

5 DISCUSSION

5.1 Surgery radiation exposure (I)

Simulations for Pt 1 and Pt 2 showed expected mean absorbed dose rates (with 0.4 mm shielding plastic material) of 39 mSv h⁻¹ and 47 mSv h⁻¹, respectively. The corresponding measurements on resected tumour tissue for Pt 1 and Pt 2 showed mean absorbed dose rates of 45 mSv h⁻¹ for both patients. The simulations thus underestimate the absorbed dose rate for Pt 1 (-13%) and overestimate the absorbed dose rate for Pt 2 (+4%). The deflections are not severe, however. The maximum absorbed dose rate on the tumour surface was about twice the simulated absorbed dose rate, assuming homogeneous activity distribution. As the surgeon is expected to move the fingers during surgery, the mean absorbed dose rate to the surgeon's fingers during complete surgery is expected to be closer to the mean than to the maximum absorbed dose rate.

5.2 NL tissue activity distributions (II,III)

5.2.1 Macroscopic distribution

The acquired autoradiograms, showing non-uniform distributions and different-sized aggregations (hot spots) and areas lacking activity (cold spots), showed indications of a heterogeneous three-dimensional distribution of both activity and absorbed dose. This is in accordance with various previous reports, on distributions in human and animal tissue (Kennedy et al. 2004, Burton et al. 1989, Campbell et al. 2000, Roberson et al. 1992, Pillai et al. 1991), described in section 1.4.4. The mentioned studies were, however, either concentrated on tumour tissue or on limited volumes of NL tissue. Furthermore, no systematic three-dimensional analysis of microsphere or absorbed dose distributions was performed on NL tissue.

The advantage of investigating radioactive tissue (Paper II) was that samples from a relatively large volume could be analysed, in a rapid and feasible way. Apart from the mentioned overview with autoradiography, activity measurements of tissue volumes made it possible to obtain a better three-dimensional description of the distribution. Furthermore, it was possible to show whether the heterogeneous activity was distributed in a larger repetitive pattern, than could be homogenised considerably by cross-fire or not. According to assumptions in Section 1.4.4, extensive heterogeneity will occur if the repetitive pattern is larger than $2.5 \times 2.5 \times 2.5 \text{ mm}^3 = 16 \text{ mm}^3$ (i.e. a

mass of 16 mg NL tissue). The heterogeneity pattern was investigated by calculation of CV and SK for the activity concentration; the assumption was that both CV and SK would decrease considerably with increasing punch biopsy mass, should the heterogeneity pattern be the same size or larger than the individual punch biopsies within the biopsy group with the largest punch biopsy mass. As mentioned in Paper II, it was hard to apply this analysis method to Pt 1, with no consistent trends for NL tissue CV or SK, as the number of samples was small in combination with a large variation in biopsy mass for this patient. The biopsy samples of Pt 2, on the other hand, showed clear trends of striking decrease of both CV and SK with biopsy mass. As different-sized biopsies were distributed in a similar manner on a large scale, variance related to large-scale activity concentration gradients is expected to be present within all the compared biopsy mass groups. In line with the example presented in Section 3.3.2, the decreasing CV and SK with increasing mass are therefore expected to be explained by heterogeneity on a scale referred to in this work as on a *macroscopic scale* (2.5–20 mm), rather than on a *large scale* (> 2 cm).

5.2.2 Small-scale distribution

The smaller sample of punch biopsies investigated by light microscopy (Paper II) provided indications of cluster gatherings and the simplified method used revealed cluster sizes < 60 spheres per cluster. In order to investigate the occurrence of even larger clusters and the possible relation between cluster size and MAD, better sectioning orientation (transversal to vessels) was applied, larger total volumes of each punch sample were scrutinised and biopsies spanning over a wider range of MAD were collected (Paper III). The latter study revealed 11 clusters > 60 spheres per cluster, and 40% of the total number of 3888 spheres found, within totally 240 sections of 16 punch biopsies, were lodged within these 11 very large clusters, the three largest clusters (i.e. 174, 306 and 453 spheres per cluster) found within the three biopsies with the highest MAD, i.e. 59, 61 and 84 Gy.

Figures 8B and 9 show that individual size of the 277 found clusters is strongly correlated with arterial diameter (for further details, see Paper III) and that the abundance of larger clusters (in larger arterioles/arteries) is increasing exponentially with increasing MAD. This implies that a high MAD often is a direct consequence of the occurrence of at least one very large or several smaller clusters.

5.3 Simulated absorbed dose (III)

The simulations of absorbed dose distributions within the 16 simulated sub-volumes, based on microsphere distributions within the punch biopsies, showed that the intrinsic non-uniformity in microsphere distribution was not homogenised, to any larger extent, by cross-fire. The increasing CV of small-scale absorbed dose with MAD demonstrates a direct consequence of the exponentially increasing cluster sizes with activity concentration, discussed in section 5.2.2. As showed by the increasing CV with activity concentration (or MAD, when assuming CPE) it is expected that the absorbed dose distribution within sub-volumes with a moderate or high MAD (the absorbed dose interval being radiobiologically interesting, when investigating heterogeneity effects), is influenced by strong absorbed dose gradients, and caused by occurrence of large clusters.

5.4 Arterial tree model simulations (IV)

5.4.1 Microsphere distribution

The simulation of microsphere distributions resulted in sphere aggregations throughout different artery generations, implying single spheres and smaller conglomerates of spheres in higher generations (i.e. with smaller diameter) and larger clusters in lower artery generations (i.e. with larger diameter). These simulations showed the influence of geometric variance, both regarding diameters within artery generations and in microsphere diameters. For the highest concentration of microspheres (28 microspheres/mg), the simulations indicated an even higher tendency for large clusters than observed in biopsies. However, it is possible that the total thickness of the sequential sections (15 sections, 450 μm in total) was not large enough to determine the complete extent of some large (50-100 microspheres/cluster) or very large (> 100 microspheres/cluster) clusters.

In the proposed model, the microspheres were assumed to be transported through the hepatic tree until entrapment, due to spatial constraints in the vessels. Furthermore, it was assumed that the variations may be described by the ACV parameter, which is normally distributed and inherently includes specific factors that influence the entrapment probabilities of the microspheres to various degrees. The simulations showed that ACV increases with increasing microsphere density, perhaps due to the random trapping process alone. Alternatively, this observation may reflect that the native artery tree structure deviates more from the simplified dichotomous bifurcation model in terms of the total variation. In addition, the used dichotomous bifurcation model returned an HDV of 130 cm^3 for the low

concentration of microspheres and 20 cm^3 for high concentration, indicating that the model does not effectively capture the whole liver. This is understandable, however, since the number of arteries generated by the dichotomous bifurcation model is far lower than the estimated number of arteries in a native liver (Debbaut et al. 2014). A decreased HDV for high microsphere concentrations is equivalent to an increased number of microsphere-accessible pathways per liver volume, and hence the number of arteries approaches the number found in the native polyfurcation model of the liver. Increasing the microsphere concentration decreased the HDV value and increased the EMB value, of which the latter is used for modelling embolisation when vessels accumulate microspheres.

5.4.2 Absorbed dose distribution

The simulated absorbed dose distributions showed geometric patterns with CV for absorbed dose increasing with increasing MAD, implying large absorbed dose gradients in regions with higher MAD, in agreement with assumptions originating from the biopsy investigations. Figure 14D-F illustrates that the occurrence of large clusters in high MAD regions has a considerable impact, not only on absorbed dose variation for samples divided into voxels. The heterogeneity remains for sub-layer MAD, i.e. when sub-layers of the total MAD volume are considered sample elements.

5.5 Clinical implications (II,III,IV)

Cremonesi et al (Cremonesi et al. 2014) recently pointed out challenges in quantification of radiobiological risks in RE treatment and that threshold absorbed doses avoiding NL toxicity are not conclusively defined. They explained that the reason for this is lack of methodological differentiation of tumour and NL tissue absorbed dose, both for glass spheres and for the most common resin sphere administration method, i.e. the Body Surface Area (BSA) method. Furthermore, detailed dosimetric follow-up studies targeting NL toxicity (Gulec et al. 2007, Lau et al. 1998) and NTCP modelling (Chiesa et al. 2012, Strigari et al. 2010, Walrand et al. 2014b) are rare (See section 1.4.3).

Absorbed dose heterogeneity on a large scale has been reported for both glass and resin spheres, using various imaging methods (Kao et al. 2013a, D'Arienzo et al. 2012, D'Arienzo et al. 2013, Sarfaraz et al. 2003, Sarfaraz et al. 2004). In the present thesis, heterogeneity on a macroscopic scale (larger than the mean range of the ^{90}Y β -radiation) was studied and the heterogeneity was found to be on an even larger scale, though perhaps not on a large enough scale for imaging, implying the presence of absorbed dose variations

that cannot be detected with non-invasive imaging methods. The scale is too large, however, for any considerable cross-fire homogenisation effects to influence the absorbed dose heterogeneity pattern.

Dosimetry on a small and even microscopic level is important, however, in order to create more complete and reliable models, capable of describing radiobiological risks. The reason for this is that microscopic or small-scale heterogeneity, combined with macroscopic heterogeneity, will reveal the total potential for radiobiological sparing of parenchyma, as some fractions of the biopsies receiving a high absorbed dose on the scale of several millimetres (macroscopically), could still contain sub-volumes of lower absorbed dose.

As mentioned in sections 1.4.4 and 1.6, some authors have described small-scale microsphere and absorbed dose distributions within NL tissue, both by investigations of explanted liver tissue (Fox et al. 1991, Burton et al. 1989) and by simulations (Gulec et al. 2010, Walrand et al. 2014a), demonstrating microsphere concentration dependent heterogeneity. The tissue volumes investigated have been small, making it hard to evaluate the representativeness of their results. The computer model by Gulec et al, assuming homogeneous microsphere distribution, demonstrated structural differences in absorbed dose, i.e. when comparing different structures. The absorbed doses did, however, not vary within the total volume of the same structures, i.e. no variation in absorbed dose was found within PT, the central veins or within the parenchyma. This is plausible, as no distributional or stochastic variations were introduced in their model. The model by Walrand et al, including some distribution heterogeneity, demonstrated absorbed dose heterogeneity only for distributions with a low total number of spheres (i.e. typically for glass sphere RE). The NL tissue and simulation investigations, accounted for in the present work, may nuance this assumption and possibly incentivise new approaches for NTCP modelling in RE therapy.

Although some sub-regions of biopsies with high MAD suffer extreme absorbed dose levels, other sub-regions may experience radiobiologically tolerable absorbed dose levels. The total biological outcome of this phenomenon is uncertain, however, as embolisation by large microsphere aggregations may either induce sub-regions of low absorbed dose and beneficial hypoxia (radioresistance) or cause cell death (necrosis) by extensive hypoxia (Lagerlöf et al. 2014). The latter effect would in that case be explained by the combination of embolisation effects in the artery and radiobiologically obstructive effects on the vein/venule within the same PT, thereby halting practically all blood supply to the parenchyma sub-volume. The size of such regions would depend on cluster size, as larger clusters are

located in lower artery generations, i.e. with a larger diameter, thus supplying blood to a larger NL volume.

The decreased HDV for high microsphere concentrations makes the present model useful for small-scale analysis, but macro-analysis of microsphere distributions in specific liver segments with volumes as low as 20 cm^3 should include data from imaging methods such as SPECT or positron emission tomography (See section 1.5.2). The combined knowledge of large-scale (from imaging) and small-scale distributions derived from the present work may be beneficial in improving NTCP models for RE.

Even though healthy parts of liver parenchyma are expected to be similar within and between patients (see section 1.1.1), the inclusion of more patients and larger tissue elements (more sections per biopsy) and samples (more elements per sample) would assure a better representativeness of the presented results. It is probable that inclusion of more data would modify the model input to some extent, e.g. by encounters of even larger clusters than the ones found in the present investigations and/or an otherwise modified distribution pattern, hence prompting adaptations of input parameters for the arterial tree model.

“There is no sense in being precise when you do not even know what you are talking about”

-John von Neumann

6 CONCLUSIONS

6.1 Surgery radiation exposure (I)

The comparison of simulations to TLD measurements shows Varskin Mod 2 to be a promising tool in predicting average tumour surface absorbed dose rates. A surgeon performing liver surgery on patients still radioactive from RE treatment should be classified (Category A) radiation worker. Pre-surgical simulations based on the planned procedure are recommended. It is also recommended that surgeons wear finger dosimeters. Given the simulated and measured absorbed dose rates, it is expected that a surgeon can perform about three surgeries of the reported kind, before approaching the annual absorbed dose limit to the hands (Directive 1996).

6.2 Microsphere distribution (II,III,IV)

6.2.1 Macroscopic distribution (II)

The trends of decreasing CV and SK with increasing biopsy mass demonstrate that a macroscopic heterogeneous pattern is expected to be present, within NL, on a relevant geometric scale, considering the mean range of the ^{90}Y β -radiation spectrum. The method of measuring absorbed dose distribution on a sample of punch biopsies is a quick and feasible method in order to describe ex-vivo macroscopic absorbed dose distribution. The method further demonstrates that autoradiography may be used for a two-dimensional overview of activity distribution, but the range of the β -radiation makes the punch biopsy measurements more reliable for a rigorous evaluation of absorbed dose distribution.

6.2.2 Small-scale distribution (II,III,IV)

Microsphere cluster aggregations and cluster size increased exponentially with microsphere concentration. A strong relation was found between cluster size and artery cross-section diameter. This indicates increasing heterogeneity in terms of an increased variation in activity concentration within individual punch biopsies, with increasing biopsy MAD. The investigated geometric heterogeneity scale, i.e. $> 16 \text{ mm}^3$, is expected to be large enough for the demonstrated heterogeneity in activity distribution to cause absorbed dose non-uniformity within individual biopsies.

6.2.3 Simulated distribution (IV)

The simulations of microsphere distributions resulted in cluster aggregations in different artery generations. Most microspheres were found within the 17th and 18th generation, consistent with a large number of mid-size and some larger clusters, in agreement with the microsphere aggregations found in punch biopsy sections. The results demonstrate that simulations from a dichotomous bifurcation model of the hepatic tree agree with microsphere distributions measured in liver samples, at least within NL sub-volumes. As mentioned in section 1.6, the dichotomous bifurcation artery tree is, however, a simplified model of a native hepatic artery tree, explaining the diminished small-scale variations with increasing simulated volume. The present model should therefore be limited to simulations within a limited fraction of the total NL parenchyma, particularly when the end point is a relatively high MAD.

6.3 Absorbed dose distribution (III,IV)

CV of absorbed dose increased with MAD, implying considerable absorbed dose heterogeneity, explained by increased fraction of spheres found in clusters and increased occurrence of larger clusters with increasing sphere concentration (or MAD, assuming CPE). The consequence of this was strong absorbed dose gradients within NL tissue within moderate and high MAD sub-volumes.

6.4 Clinical implications (II,III,IV)

The results reported in the present thesis, with large cluster lodgings outside the highest generations (i.e. outside the terminal, thinnest, arterioles) of the hepatic arterial tree, both as found in biopsies and by simulations, resulting in considerable absorbed dose non-uniformity, may challenge the hypotheses of limited absorbed dose heterogeneity for resin sphere RE. Strong absorbed dose gradients within individual biopsies will result in a systematic absorbed dose inhomogeneity, which may be beneficial for both parenchyma and other critical structures, with sub-volumes receiving a high absorbed dose, such as the PT. The decreased HDV for high microsphere concentrations makes our model useful for small-scale analysis, but macro-analysis of microsphere distributions in specific liver segments with volumes as low as 20 cm³ should include large-scale data. Therefore, imaging via SPECT/CT and PET/CT in combination with small-scale modelling may enable the use of small-scale dosimetry to determine SIRT tolerability and NTCP modelling. The total biologic outcome of large clusters should, however, be examined further, in

order to determine if the low absorbed dose for high MAD sub-regions is beneficial or if these sub-regions will suffer fatal consequences of extensive hypoxia leading to necrosis, caused by the combination of embolisation effects and the potentially radiobiologically obstructive influence on nearby portal venules/veins.

“The future is no more uncertain than the present”

-Walter Whitman

7 FUTURE PERSPECTIVES

The papers presented in this thesis have, by providing new information about microsphere and absorbed dose distributions in RE, opened up for better radiobiological modelling and optimisation of administration methods.

It would be of clinical value to simulate the influence of variation of physical parameters such as microsphere diameter, total number of injected spheres, activity per sphere and also radionuclide and study how this may change the sphere and absorbed dose distribution parameters, e.g. CV and SK.

The distribution parameters should be verified by inclusion of more tissue data, hence possibly prompting adaptations of input parameters for the arterial tree model.

Furthermore, comparison of biomarker expressions (Guha and Kavanagh 2011) at different distance to microsphere aggregations of different size, therefore depending on absorbed dose and structural sensitivity, would be valuable input, in order to explain toxicity mechanisms.

It is also possible that tumour modelling (Lagerlöf et al. 2014) may provide possible application of the arterial tree model to tumour regions, with less adaptations for smaller tumours, as the morphology and vascularisation of such tumours are expected to be more similar to NL tissue than the more amorphous structure and chaotic vascularisation present in larger tumours (Milross et al. 1997).

Finally, it would be of interest to simulate the influence of embolisation and radiobiological effects caused by large clusters. The aim would be to distinguish i) benefits of sub-regional low absorbed dose and radiation insensitivity caused by limited hypoxia from ii) too high a degree of hypoxia, leading to cell death (necrosis) within NL tissue, induced by the combination of embolisation effects and obstructive radiobiological damages to venules/veins within the PTs containing large microsphere clusters.

“... people will forget what you said, people will forget what you did, but people will never forget how you made them feel”

-Maya Angelou

ACKNOWLEDGEMENTS

This work was supported by grants from the Swedish National Cancer Society, the Swedish Radiation Safety Authority and King Gustav V Jubilee Clinic Cancer Research Foundation.

I am grateful for having had the opportunity to work with experienced and skilful professionals from different medical disciplines. Without them, my family and friends, this work would not have been possible.

First of all, I thank my main supervisor, Peter Bernhardt, for introducing me to scientific work, for inspiring words, for his positive and visionary mind, friendship and passion for research; you are truly an extraordinary person, both intellectually and emotionally. I feel privileged having worked with you and I have enjoyed it very much. I am also grateful to Ragnar Hultborn, my co-supervisor, for his always enthusiastic attitude and contagious interest for interdisciplinary research; you have been a great source of inspiration and have provided very important scientific advice and article text contributions. I thank my other skilful co-authors, Magnus Rizell, Johanna Svensson, Olof Henrikson, Johan Mölne and Peter Gjertsson, for their work, our scientific conversations and their text contributions. Among them, special thanks to Johanna; your uplifting words and positive attitude have been important to me. I thank Jakob Himmelman, for insightful conversations about physics and many other things. Thank you, also, Emma Wikberg and Rebecca Hermann, for the good cooperation and all the fun moments.

I thank my highly gifted and big-hearted colleagues, Jakob Heydorn Lagerlöf and Tobias Magnander, for all that you have done for me, intellectually, scientifically, but most of all, emotionally, making every day at work encouraging, inspiring, fun and sometimes a little crazy. You both mean a lot to me. Thank you, Jakob, for being my dear friend and excellent roommate, always witty and reliable and for bringing order to my sometimes too philosophical and distracted mind. Thank you for experienced help with Matlab, as well. Thank you, Tobias, for being my close friend and a constant source of encouragement, in your cheerful, frank and generous personality. It is always fun being around you.

I thank all my colleagues at the Department of Radiation Physics and DrÄG. I will remember many fun moments, especially with Anders, Anna, Britta, Christina, Elin, Emil, Emma, Ingun, Johanna D, Maria, Micke, Niclas, Nils, Jenny, Joel, Johan, Sara and Viktor. I am also grateful to the staff at the Department of Medical Physics and Biomedical Engineering (“MFT”) and at the Department of Nuclear Medicine – working with you all has been a pleasure – and also to all students, making teaching joyful.

My final gratitude goes to all supportive and caring relatives and friends, and to my beloved family: my father and mother, Jan and Rose-Marie, for your love and for always being there for me, my brothers, Simon and Jacob, for your positive, fun and warm personalities, making me proud to be your brother, and to my amazing wife, Nerea - thank you for being who you are, with your loving and caring personality; thank you for making me happy, giving my life meaning, for your great sense of humour - helping you to cope with my shortcomings, and thank you for making me feel treasured and unique. I love you so much.

Jonas Högberg, Göteborg, 12 April 2015

“My idea of an agreeable person is a person who agrees with me”

-Benjamin Disraeli

REFERENCES

- Ahmadzadehfar, H., H. Duan, A. R. Haug, S. Walrand & M. Hoffmann (2014) The role of SPECT/CT in radioembolization of liver tumours. *European journal of nuclear medicine and molecular imaging*, 41 Suppl 1, S115-24.
- Ahmadzadehfar, H., M. Muckle, A. Sabet, K. Wilhelm, C. Kuhl, K. Biermann, T. Haslerud, H. J. Biersack & S. Ezziddin (2011a) The significance of bremsstrahlung SPECT/CT after yttrium-90 radioembolization treatment in the prediction of extrahepatic side effects. *European journal of nuclear medicine and molecular imaging*.
- Ahmadzadehfar, H., A. Sabet, K. Biermann, M. Muckle, H. Brockmann, C. Kuhl, K. Wilhelm, H. J. Biersack & S. Ezziddin (2010) The significance of ^{99m}Tc -MAA SPECT/CT liver perfusion imaging in treatment planning for ^{90}Y -microsphere selective internal radiation treatment. *Journal of nuclear medicine : official publication, Society of Nuclear Medicine*, 51, 1206-12.
- Ahmadzadehfar, H., A. Sabet, M. Muckle, K. Wilhelm, K. Reichmann, H. J. Biersack & S. Ezziddin (2011b) ^{99m}Tc -MAA/ ^{90}Y -Bremsstrahlung SPECT/CT after simultaneous Tc-MAA/ ^{90}Y -microsphere injection for immediate treatment monitoring and further therapy planning for radioembolization. *European journal of nuclear medicine and molecular imaging*, 38, 1281-8.
- Aljiffry, M., M. J. Walsh & M. Molinari (2009) Advances in diagnosis, treatment and palliation of cholangiocarcinoma: 1990-2009. *World journal of gastroenterology : WJG*, 15, 4240-62.
- Basciano, C. A., C. Kleinstreuer, A. S. Kennedy, W. A. DeZarn & E. Childress (2010) Computer modeling of controlled microsphere release and targeting in a representative hepatic artery system. *Annals of biomedical engineering*, 38, 1862-79.
- Bruix, J. & M. Sherman (2011) Management of hepatocellular carcinoma: an update. *Hepatology*, 53, 1020-2.
- Burton, M. A., B. N. Gray, P. F. Klemp, D. K. Kelleher & N. Hardy (1989) Selective internal radiation therapy: distribution of radiation in the liver. *European journal of cancer & clinical oncology*, 25, 1487-91.
- Campbell, A. M., I. H. Bailey & M. A. Burton (2000) Analysis of the distribution of intra-arterial microspheres in human liver following hepatic yttrium-90 microsphere therapy. *Physics in medicine and biology*, 45, 1023-33.
- Carmeliet, P. & R. K. Jain (2000) Angiogenesis in cancer and other diseases. *Nature*, 407, 249-57.
- Chen, Y. X., Z. C. Zeng, Z. Y. Tang, J. Fan, J. Zhou, W. Jiang, M. S. Zeng & Y. S. Tan (2010) Determining the role of external beam radiotherapy

- in unresectable intrahepatic cholangiocarcinoma: a retrospective analysis of 84 patients. BMC cancer, 10, 492.*
- Chiesa, C., M. Mira, M. Maccauro, R. Romito, C. Spreafico, C. Sposito, S. Bhoori, C. Morosi, S. Pellizzari, A. Negri, E. Civelli, R. Lanocita, T. Camerini, C. Bampo, M. Carrara, E. Seregini, A. Marchiano, V. Mazzaferro & E. Bombardieri (2012) *A dosimetric treatment planning strategy in radioembolization of hepatocarcinoma with 90Y glass microspheres. The quarterly journal of nuclear medicine and molecular imaging : official publication of the Italian Association of Nuclear Medicine, 56, 503-8.*
- Chua, T. C., L. Bester, A. Saxena & D. L. Morris (2011) *Radioembolization and systemic chemotherapy improves response and survival for unresectable colorectal liver metastases. Journal of cancer research and clinical oncology, 137, 865-73.*
- Crawford, A. R., X. Z. Lin & J. M. Crawford (1998) *The normal adult human liver biopsy: a quantitative reference standard. Hepatology, 28, 323-31.*
- Cremonesi, M., C. Chiesa, L. Strigari, M. Ferrari, F. Botta, F. Guerriero, C. De Cicco, G. Bonomo, F. Orsi, L. Bodei, A. Di Dia, C. M. Grana & R. Orecchia (2014) *Radioembolization of hepatic lesions from a radiobiology and dosimetric perspective. Frontiers in oncology, 4, 210.*
- Cremonesi, M., M. Ferrari, M. Bartolomei, F. Orsi, G. Bonomo, D. Arico, A. Mallia, C. De Cicco, G. Pedroli & G. Paganelli (2008) *Radioembolisation with 90Y-microspheres: dosimetric and radiobiological investigation for multi-cycle treatment. European journal of nuclear medicine and molecular imaging, 35, 2088-96.*
- Cremonesi, M., M. Ferrari, L. Bodei, G. Tosi & G. Paganelli (2006) *Dosimetry in Peptide radionuclide receptor therapy: a review. Journal of nuclear medicine : official publication, Society of Nuclear Medicine, 47, 1467-75.*
- D'Arienzo, M., P. Chiaramida, L. Chiacchiararelli, A. Coniglio, R. Cianni, R. Salvatori, A. Ruzza, F. Scopinaro & O. Bagni (2012) *90Y PET-based dosimetry after selective internal radiotherapy treatments. Nuclear medicine communications, 33, 633-40.*
- D'Arienzo, M., L. Filippi, P. Chiaramida, L. Chiacchiararelli, R. Cianni, R. Salvatori, F. Scopinaro & O. Bagni (2013) *Absorbed dose to lesion and clinical outcome after liver radioembolization with 90Y microspheres: a case report of PET-based dosimetry. Annals of nuclear medicine, 27, 676-80.*
- Dale, R. G. (1985) *The application of the linear-quadratic dose-effect equation to fractionated and protracted radiotherapy. The British journal of radiology, 58, 515-28.*
- Dale, R. G. & B. Jones. 2007. *Radiobiological modelling in radiation oncology. 65. London: British Institute of Radiology.*

- Dawson, L. A., D. Normolle, J. M. Balter, C. J. McGinn, T. S. Lawrence & R. K. Ten Haken (2002) Analysis of radiation-induced liver disease using the Lyman NTCP model. *International journal of radiation oncology, biology, physics*, 53, 810-21.
- Debbaut, C., P. Segers, P. Cornillie, C. Casteleyn, M. Dierick, W. Laleman & D. Monbaliu (2014) Analyzing the human liver vascular architecture by combining vascular corrosion casting and micro-CT scanning: a feasibility study. *Journal of anatomy*, 224, 509-17.
- Dhabuwala, A., P. Lamerton & R. S. Stubbs (2005) Relationship of ^{99m}technetium labelled macroaggregated albumin (^{99m}Tc-MAA) uptake by colorectal liver metastases to response following Selective Internal Radiation Therapy (SIRT). *BMC nuclear medicine*, 5, 7.
- Directive, C. (1996) 96/29/Euratom of 13 May 1996 laying down basic safety standards for the protection of the health of workers and the general public against the dangers arising from ionizing radiation. *Official Journal of the European Communities*, 39.
- Doane, D. P. & L. W. Seward. 2013. *Applied statistics in business and economics*. New York: McGraw-Hill/Irwin.
- Elschot, M., J. F. Nijsen, A. J. Dam & H. W. de Jong (2011) Quantitative evaluation of scintillation camera imaging characteristics of isotopes used in liver radioembolization. *PloS one*, 6, e26174.
- Elschot, M., B. J. Vermolen, M. G. Lam, B. de Keizer, M. A. van den Bosch & H. W. de Jong (2013) Quantitative comparison of PET and Bremsstrahlung SPECT for imaging the in vivo yttrium-90 microsphere distribution after liver radioembolization. *PloS one*, 8, e55742.
- Emami, B., J. Lyman, A. Brown, L. Coia, M. Goitein, J. E. Munzenrider, B. Shank, L. J. Solin & M. Wesson (1991) Tolerance of normal tissue to therapeutic irradiation. *International journal of radiation oncology, biology, physics*, 21, 109-22.
- Ferrara, N., H. P. Gerber & J. LeCouter (2003) The biology of VEGF and its receptors. *Nature medicine*, 9, 669-76.
- Flamen, P., B. Vanderlinden, P. Delatte, G. Ghanem, L. Ameye, M. Van Den Eynde & A. Hendlisz (2008) Multimodality imaging can predict the metabolic response of unresectable colorectal liver metastases to radioembolization therapy with Yttrium-90 labeled resin microspheres. *Physics in medicine and biology*, 53, 6591-603.
- Fox, R. A., P. F. Klemp, G. Egan, L. L. Mina, M. A. Burton & B. N. Gray (1991) Dose distribution following selective internal radiation therapy. *International journal of radiation oncology, biology, physics*, 21, 463-7.
- Fuss, M., B. J. Salter, T. S. Herman & C. R. Thomas, Jr. (2004) External beam radiation therapy for hepatocellular carcinoma: potential of intensity-modulated and image-guided radiation therapy. *Gastroenterology*, 127, S206-17.

- Gandhi, S. J., S. Babu, P. Subramanyam & P. Shanmuga Sundaram (2013) *Tc-99m macro aggregated albumin scintigraphy - indications other than pulmonary embolism: A pictorial essay. Indian journal of nuclear medicine : IJNM : the official journal of the Society of Nuclear Medicine, India, 28, 152-62.*
- Goin, J. E., R. Salem, B. I. Carr, J. E. Dancey, M. C. Soulen, J. F. Geschwind, K. Goin, M. Van Buskirk & K. Thurston (2005) *Treatment of unresectable hepatocellular carcinoma with intrahepatic yttrium 90 microspheres: factors associated with liver toxicities. Journal of vascular and interventional radiology : JVIR, 16, 205-13.*
- Guha, C. & B. D. Kavanagh (2011) *Hepatic radiation toxicity: avoidance and amelioration. Seminars in Radiation Oncology, 21, 256-63.*
- Gulec, S. A., G. Mesoloras, W. A. Dezarn, P. McNeillie & A. S. Kennedy (2007) *Safety and efficacy of Y-90 microsphere treatment in patients with primary and metastatic liver cancer: the tumor selectivity of the treatment as a function of tumor to liver flow ratio. Journal of translational medicine, 5, 15.*
- Gulec, S. A., M. L. Szejnberg, J. A. Siegel, T. Jevremovic & M. Stabin (2010) *Hepatic structural dosimetry in (90)Y microsphere treatment: a Monte Carlo modeling approach based on lobular microanatomy. Journal of nuclear medicine : official publication, Society of Nuclear Medicine, 51, 301-10.*
- Hall, E. J. & D. J. Brenner (1992) *The dose-rate effect in interstitial brachytherapy: a controversy resolved. The British journal of radiology, 65, 242-7.*
- Hamami, M. E., T. D. Poeppel, S. Muller, T. Heusner, A. Bockisch, P. Hilgard & G. Antoch (2009) *SPECT/CT with 99mTc-MAA in radioembolization with 90Y microspheres in patients with hepatocellular cancer. Journal of nuclear medicine : official publication, Society of Nuclear Medicine, 50, 688-92.*
- Haug, A. R., V. Heinemann, C. J. Bruns, R. Hoffmann, T. Jakobs, P. Bartenstein & M. Hacker (2011) *18F-FDG PET independently predicts survival in patients with cholangiocellular carcinoma treated with 90Y microspheres. European journal of nuclear medicine and molecular imaging, 38, 1037-45.*
- Ho, S., W. Y. Lau, T. W. Leung, M. Chan, K. W. Chan, W. Y. Lee, P. J. Johnson & A. K. Li (1997) *Tumour-to-normal uptake ratio of 90Y microspheres in hepatic cancer assessed with 99Tcm macroaggregated albumin. The British journal of radiology, 70, 823-8.*
- Ho, S., W. Y. Lau, T. W. Leung & P. J. Johnson (1998) *Internal radiation therapy for patients with primary or metastatic hepatic cancer: a review. Cancer, 83, 1894-907.*

- Ingold, J. A., G. B. Reed, H. S. Kaplan & M. A. Bagshaw (1965) Radiation Hepatitis. *The American journal of roentgenology, radium therapy, and nuclear medicine*, 93, 200-8.
- Jemal, A., F. Bray, M. M. Center, J. Ferlay, E. Ward & D. Forman (2011) Global cancer statistics. *CA: a cancer journal for clinicians*, 61, 69-90.
- Jung, J., S. M. Yoon, S. Y. Kim, B. Cho, J. H. Park, S. S. Kim, S. Y. Song, S. W. Lee, S. D. Ahn, E. K. Choi & J. H. Kim (2013) Radiation-induced liver disease after stereotactic body radiotherapy for small hepatocellular carcinoma: clinical and dose-volumetric parameters. *Radiation oncology*, 8, 249.
- Kao, Y. H., A. E. Hock Tan, M. C. Burgmans, F. G. Irani, L. S. Khoo, R. H. Gong Lo, K. H. Tay, B. S. Tan, P. K. Hoe Chow, D. C. Eng Ng & A. S. Whatt Goh (2012) Image-guided personalized predictive dosimetry by artery-specific SPECT/CT partition modeling for safe and effective ⁹⁰Y radioembolization. *Journal of nuclear medicine : official publication, Society of Nuclear Medicine*, 53, 559-66.
- Kao, Y. H., J. D. Steinberg, Y. S. Tay, G. K. Lim, J. Yan, D. W. Townsend, C. A. Budgeon, J. A. Boucek, R. J. Francis, T. S. Cheo, M. C. Burgmans, F. G. Irani, R. H. Lo, K. H. Tay, B. S. Tan, P. Chow, S. Satchithanatham, A. E. Tan, D. C. Ng & A. S. Goh (2013a) Post-radioembolization yttrium-90 PET/CT - part 2: dose-response and tumor predictive dosimetry for resin microspheres. *EJNMMI research*, 3, 57.
- Kao, Y. H., J. D. Steinberg, Y. S. Tay, G. K. Lim, J. Yan, D. W. Townsend, A. Takano, M. C. Burgmans, F. G. Irani, T. K. Teo, T. N. Yeow, A. Gogna, R. H. Lo, K. H. Tay, B. S. Tan, P. Chow, S. Satchithanatham, A. E. Tan, D. C. Ng & A. S. Goh (2013b) Post-radioembolization yttrium-90 PET/CT - part 1: diagnostic reporting. *EJNMMI research*, 3, 56.
- Kao, Y. H., E. H. Tan, C. E. Ng & S. W. Goh (2011a) Clinical implications of the body surface area method versus partition model dosimetry for yttrium-90 radioembolization using resin microspheres: a technical review. *Annals of nuclear medicine*, 25, 455-61.
- (2011b) Yttrium-90 time-of-flight PET/CT is superior to Bremsstrahlung SPECT/CT for postradioembolization imaging of microsphere biodistribution. *Clinical nuclear medicine*, 36, e186-7.
- Kassis, A. I. & S. J. Adelstein (2005) Radiobiologic principles in radionuclide therapy. *Journal of nuclear medicine : official publication, Society of Nuclear Medicine*, 46 Suppl 1, 4S-12S.
- Kennedy, A. S., C. Kleinstreuer, C. A. Basciano & W. A. Dezarn (2010) Computer modeling of yttrium-90-microsphere transport in the hepatic arterial tree to improve clinical outcomes. *International journal of radiation oncology, biology, physics*, 76, 631-7.

- Kennedy, A. S., P. McNeillie, W. A. Dezarn, C. Nutting, B. Sangro, D. Wertman, M. Garafalo, D. Liu, D. Coldwell, M. Savin, T. Jakobs, S. Rose, R. Warner, D. Carter, S. Sapareto, S. Nag, S. Gulec, A. Calkins, V. L. Gates & R. Salem (2009) Treatment parameters and outcome in 680 treatments of internal radiation with resin ^{90}Y -microspheres for unresectable hepatic tumors. *International journal of radiation oncology, biology, physics*, 74, 1494-500.
- Kennedy, A. S., C. Nutting, D. Coldwell, J. Gaiser & C. Drachenberg (2004) Pathologic response and microdosimetry of (^{90}Y) microspheres in man: review of four explanted whole livers. *International journal of radiation oncology, biology, physics*, 60, 1552-63.
- Khokha, M. K., G. Landini & P. M. Iannaccone (1994) Fractal geometry in rat chimeras demonstrates that a repetitive cell division program may generate liver parenchyma. *Developmental biology*, 165, 545-55.
- Kim, J. H., H. J. Won, Y. M. Shin, K. A. Kim & P. N. Kim (2011) Radiofrequency ablation for the treatment of primary intrahepatic cholangiocarcinoma. *AJR. American journal of roentgenology*, 196, W205-9.
- King, A. W., A. R. Johnson & R. V. O'Neill (1991) Transmutation and functional representation of heterogeneous landscapes. *Landscape Ecology*, 5, 239-253.
- Kiskowski, M. A., J. F. Hancock & A. K. Kenworthy (2009) On the use of Ripley's K-function and its derivatives to analyze domain size. *Biophysical journal*, 97, 1095-103.
- Knapp, F. F., Jr., A. L. Beets, S. Guhlke, P. O. Zamora, H. Bender, H. Palmedo & H. J. Biersack (1997) Availability of rhenium-188 from the alumina-based tungsten-188/rhenium-188 generator for preparation of rhenium-188-labeled radiopharmaceuticals for cancer treatment. *Anticancer research*, 17, 1783-95.
- Knesaurek, K., J. Machac, M. Muzinic, M. DaCosta, Z. Zhang & S. Heiba (2010) Quantitative comparison of yttrium-90 (^{90}Y)-microspheres and technetium-99m ($^{99\text{m}}\text{Tc}$)-macroaggregated albumin SPECT images for planning ^{90}Y therapy of liver cancer. *Technology in cancer research & treatment*, 9, 253-62.
- Kodina, G., G. Korpusov & A. Filyanin (2002) Production of high-purity ^{90}Y on specially developed centrifugal semicounterflow extractors. *Radiochemistry*, 44, 62-66.
- Kooby, D. A., V. Egnatashvili, S. Srinivasan, A. Chamsuddin, K. A. Delman, J. Kauh, C. A. Staley, 3rd & H. S. Kim (2010) Comparison of yttrium-90 radioembolization and transcatheter arterial chemoembolization for the treatment of unresectable hepatocellular carcinoma. *Journal of vascular and interventional radiology : JVIR*, 21, 224-30.

- Koops, A., B. Wojciechowski, D. C. Broering, G. Adam & G. Krupski-Berdien (2004) *Anatomic variations of the hepatic arteries in 604 selective celiac and superior mesenteric angiographies. Surgical and radiologic anatomy : SRA*, 26, 239-44.
- Kuvshinoff, B. & Y. Fong (2007) *Surgical therapy of liver metastases. Seminars in oncology*, 34, 177-85.
- Källman, P., A. Ågren & A. Brahme (1992) *Tumour and normal tissue responses to fractionated non-uniform dose delivery. International journal of radiation biology*, 62, 249-62.
- Lagerlöf, J. H., J. Kindblom & P. Bernhardt (2014) *The impact of including spatially longitudinal heterogeneities of vessel oxygen content and vascular fraction in 3D tumor oxygenation models on predicted radiation sensitivity. Medical physics*, 41, 044101.
- Lam, N. S. N. & D. A. Quattrochi (1992) *On the issues of scale, resolution, and fractal analysis in the mapping sciences*. The Professional Geographer*, 44, 88-98.
- Lam, V. W., C. Spiro, J. M. Laurence, E. Johnston, M. J. Hollands, H. C. Pleass & A. J. Richardson (2012) *A systematic review of clinical response and survival outcomes of downsizing systemic chemotherapy and rescue liver surgery in patients with initially unresectable colorectal liver metastases. Annals of Surgical Oncology*, 19, 1292-301.
- Lamers, W. H., A. Hilberts, E. Furt, J. Smith, G. N. Jonges, C. J. van Noorden, J. W. Janzen, R. Charles & A. F. Moorman (1989) *Hepatic enzymic zonation: a reevaluation of the concept of the liver acinus. Hepatology*, 10, 72-6.
- Lance, C., G. McLennan, N. Obuchowski, G. Cheah, A. Levitin, M. Sands, J. Spain, S. Srinivas, S. Shrikanthan, F. N. Aucejo, R. Kim & K. V. Menon (2011) *Comparative analysis of the safety and efficacy of transcatheter arterial chemoembolization and yttrium-90 radioembolization in patients with unresectable hepatocellular carcinoma. Journal of vascular and interventional radiology : JVIR*, 22, 1697-705.
- Lau, W. Y., S. Ho, T. W. Leung, M. Chan, R. Ho, P. J. Johnson & A. K. Li (1998) *Selective internal radiation therapy for nonresectable hepatocellular carcinoma with intraarterial infusion of 90yttrium microspheres. International journal of radiation oncology, biology, physics*, 40, 583-92.
- Lau, W. Y., A. S. Kennedy, Y. H. Kim, H. K. Lai, R. C. Lee, T. W. Leung, C. S. Liu, R. Salem, B. Sangro, B. Shuter & S. C. Wang (2012) *Patient selection and activity planning guide for selective internal radiotherapy with yttrium-90 resin microspheres. International journal of radiation oncology, biology, physics*, 82, 401-7.
- Leith, J. T., S. Cook, P. Chougule, P. Calabresi, L. Wahlberg, C. Lindquist & M. Epstein (1994) *Intrinsic and extrinsic characteristics of human*

- tumors relevant to radiosurgery: comparative cellular radiosensitivity and hypoxic percentages. *Acta neurochirurgica. Supplement*, 62, 18-27.
- Leung, T. W., W. Y. Lau, S. K. Ho, S. C. Ward, J. H. Chow, M. S. Chan, C. Metreweli, P. J. Johnson & A. K. Li (1995) Radiation pneumonitis after selective internal radiation treatment with intraarterial ⁹⁰yttrium-microspheres for inoperable hepatic tumors. *International journal of radiation oncology, biology, physics*, 33, 919-24.
- Lewandowski, R. J., L. M. Kulik, A. Riaz, S. Senthilnathan, M. F. Mulcahy, R. K. Ryu, S. M. Ibrahim, K. T. Sato, T. Baker, F. H. Miller, R. Omary, M. Abecassis & R. Salem (2009) A comparative analysis of transarterial downstaging for hepatocellular carcinoma: chemoembolization versus radioembolization. *American journal of transplantation : official journal of the American Society of Transplantation and the American Society of Transplant Surgeons*, 9, 1920-8.
- Lhommel, R., P. Goffette, M. Van den Eynde, F. Jamar, S. Pauwels, J. I. Bilbao & S. Walrand (2009) Yttrium-90 TOF PET scan demonstrates high-resolution biodistribution after liver SIRT. *European journal of nuclear medicine and molecular imaging*, 36, 1696.
- Llovet, J. M., M. I. Real, X. Montana, R. Planas, S. Coll, J. Aponte, C. Ayuso, M. Sala, J. Muchart, R. Sola, J. Rodes & J. Bruix (2002) Arterial embolisation or chemoembolisation versus symptomatic treatment in patients with unresectable hepatocellular carcinoma: a randomised controlled trial. *Lancet*, 359, 1734-9.
- Loew, M. H., R. L. Pickholtz, L. Goldman, F. Hill & F. Lawler. 1980. *Analysis and Development of Image Statistics and Redundancy Removal. DTIC Document.*
- Meade, V. M., M. A. Burton, B. N. Gray & G. W. Self (1987) Distribution of different sized microspheres in experimental hepatic tumours. *European journal of cancer & clinical oncology*, 23, 37-41.
- Mendez Romero, A., W. Wunderink, S. M. Hussain, J. A. De Pooter, B. J. Heijmen, P. C. Nowak, J. J. Nuyttens, R. P. Brandwijk, C. Verhoef, J. N. Ijzermans & P. C. Levendag (2006) Stereotactic body radiation therapy for primary and metastatic liver tumors: A single institution phase i-ii study. *Acta oncologica*, 45, 831-7.
- Meyer, C., C. C. Pieper, S. Ezziddin, K. E. Wilhelm, H. H. Schild & H. Ahmadzadehfar (2014) Feasibility of temporary protective embolization of normal liver tissue using degradable starch microspheres during radioembolization of liver tumours. *European journal of nuclear medicine and molecular imaging*, 41, 231-7.
- Milano, M. T., L. S. Constine & P. Okunieff (2007) Normal tissue tolerance dose metrics for radiation therapy of major organs. *Seminars in Radiation Oncology*, 17, 131-40.

- Milross, C. G., S. L. Tucker, K. A. Mason, N. R. Hunter, L. J. Peters & L. Milas (1997) The effect of tumor size on necrosis and polarographically measured pO₂. *Acta oncologica*, 36, 183-9.
- Minami, Y. & M. Kudo (2011) Radiofrequency ablation of hepatocellular carcinoma: a literature review. *International journal of hepatology*, 2011, 104685.
- Minarik, D., K. Sjogreen Gleisner & M. Ljungberg (2008) Evaluation of quantitative (90)Y SPECT based on experimental phantom studies. *Physics in medicine and biology*, 53, 5689-703.
- Nelson, K., P. E. Vause, Jr. & P. Koropova (2008) Post-mortem considerations of Yttrium-90 90Y microsphere therapy procedures. *Health physics*, 95, S156-61.
- Nowicki, M. L., J. B. Cwikla, A. J. Sankowski, S. Shcherbinin, J. Grimmes, A. Celler, J. R. Buscombe, A. Bator, M. Pech, R. Mikolajczak & D. Pawlak (2014) Initial study of radiological and clinical efficacy radioembolization using 188Re-human serum albumin (HSA) microspheres in patients with progressive, unresectable primary or secondary liver cancers. *Medical science monitor : international medical journal of experimental and clinical research*, 20, 1353-62.
- O'Doherty, J., J. Scuffham & P. Hinton (2011) The importance of scatter correction for the assessment of lung shunting prior to yttrium-90 radioembolization therapy. *Nuclear medicine communications*, 32, 628-34.
- Okada, S. (1998) Chemotherapy in hepatocellular carcinoma. *Hepato-gastroenterology*, 45 Suppl 3, 1259-63.
- Pan, C. C., B. D. Kavanagh, L. A. Dawson, X. A. Li, S. K. Das, M. Miften & R. K. Ten Haken (2010) Radiation-associated liver injury. *International journal of radiation oncology, biology, physics*, 76, S94-100.
- Pickett, S. T. & M. L. Cadenasso (1995) Landscape ecology: spatial heterogeneity in ecological systems. *Science*, 269, 331-4.
- Pillai, K. M., P. E. McKeever, C. A. Knutsen, P. A. Terrio, D. M. Prieskorn & W. D. Ensminger (1991) Microscopic analysis of arterial microsphere distribution in rabbit liver and hepatic VX2 tumor. *Selective cancer therapeutics*, 7, 39-48.
- Prestwich, W. V., J. Nunes & C. S. Kwok (1989) Beta dose point kernels for radionuclides of potential use in radioimmunotherapy. *Journal of nuclear medicine : official publication, Society of Nuclear Medicine*, 30, 1036-46.
- Qin, Y. F., M. Van Cauteren, M. Osteaux & G. Willems (1990) Determination of liver volume in vivo in rats using MRI. *European journal of radiology*, 11, 191-5.
- Rand, T., C. Loewe, M. Schoder, M. T. Schmook, M. Peck-Radosavljevic, J. Kettenbach, F. Wolf, B. Schneider & J. Lammer (2005) Arterial embolization of unresectable hepatocellular carcinoma with use of

- microspheres, lipiodol, and cyanoacrylate. Cardiovascular and interventional radiology, 28, 313-8.*
- Rappaport, A. M. (1973) *The microcirculatory hepatic unit. Microvascular research, 6, 212-28.*
- Rappaport, A. M., Z. J. Borowy, W. M. Loughheed & W. N. Lotto (1954) *Subdivision of hexagonal liver lobules into a structural and functional unit; role in hepatic physiology and pathology. The Anatomical record, 119, 11-33.*
- Riaz, A., R. Awais & R. Salem (2014) *Side effects of yttrium-90 radioembolization. Frontiers in oncology, 4, 198.*
- Riaz, A., V. L. Gates, B. Atassi, R. J. Lewandowski, M. F. Mulcahy, R. K. Ryu, K. T. Sato, T. Baker, L. Kulik, R. Gupta, M. Abecassis, A. B. Benson, 3rd, R. Omary, L. Millender, A. Kennedy & R. Salem (2011) *Radiation segmentectomy: a novel approach to increase safety and efficacy of radioembolization. International journal of radiation oncology, biology, physics, 79, 163-71.*
- Roberson, P. L., R. K. Ten Haken, D. L. McShan, P. E. McKeever & W. D. Ensminger (1992) *Three-dimensional tumor dosimetry for hepatic yttrium-90-microsphere therapy. Journal of nuclear medicine : official publication, Society of Nuclear Medicine, 33, 735-8.*
- Rong, X., Y. Du, M. Ljungberg, E. Rault, S. Vandenberghe & E. C. Frey (2012) *Development and evaluation of an improved quantitative (90)Y bremsstrahlung SPECT method. Medical physics, 39, 2346-58.*
- Salem, R. & R. J. Lewandowski (2013) *Chemoembolization and radioembolization for hepatocellular carcinoma. Clinical gastroenterology and hepatology : the official clinical practice journal of the American Gastroenterological Association, 11, 604-11; quiz e43-4.*
- Salem, R., R. J. Lewandowski, L. Kulik, E. Wang, A. Riaz, R. K. Ryu, K. T. Sato, R. Gupta, P. Nikolaidis, F. H. Miller, V. Yaghamai, S. M. Ibrahim, S. Senthilnathan, T. Baker, V. L. Gates, B. Atassi, S. Newman, K. Memon, R. Chen, R. L. Vogelzang, A. A. Nemcek, S. A. Resnick, H. B. Chrisman, J. Carr, R. A. Omary, M. Abecassis, A. B. Benson, 3rd & M. F. Mulcahy (2011) *Radioembolization results in longer time-to-progression and reduced toxicity compared with chemoembolization in patients with hepatocellular carcinoma. Gastroenterology, 140, 497-507 e2.*
- Salem, R., R. J. Lewandowski, M. F. Mulcahy, A. Riaz, R. K. Ryu, S. Ibrahim, B. Atassi, T. Baker, V. Gates, F. H. Miller, K. T. Sato, E. Wang, R. Gupta, A. B. Benson, S. B. Newman, R. A. Omary, M. Abecassis & L. Kulik (2010) *Radioembolization for hepatocellular carcinoma using Yttrium-90 microspheres: a comprehensive report of long-term outcomes. Gastroenterology, 138, 52-64.*
- Sarfaraz, M., A. S. Kennedy, Z. J. Cao, G. D. Sackett, C. X. Yu, M. A. Lodge, R. Murthy, B. R. Line & D. A. Van Echo (2003) *Physical aspects of*

- yttrium-90 microsphere therapy for nonresectable hepatic tumors. *Medical physics*, 30, 199-203.
- Sarfaraz, M., A. S. Kennedy, M. A. Lodge, X. A. Li, X. Wu & C. X. Yu (2004) Radiation absorbed dose distribution in a patient treated with yttrium-90 microspheres for hepatocellular carcinoma. *Medical physics*, 31, 2449-53.
- Saxena, R., N. D. Theise & J. M. Crawford (1999) Microanatomy of the human liver-exploring the hidden interfaces. *Hepatology*, 30, 1339-46.
- Shen, S., G. L. DeNardo & S. J. DeNardo (1994a) Quantitative bremsstrahlung imaging of yttrium-90 using a Wiener filter. *Medical physics*, 21, 1409-17.
- Shen, S., G. L. DeNardo, A. Yuan, D. A. DeNardo & S. J. DeNardo (1994b) Planar gamma camera imaging and quantitation of yttrium-90 bremsstrahlung. *Journal of nuclear medicine : official publication, Society of Nuclear Medicine*, 35, 1381-9.
- Sherbini, S., J. DeCicco, A. T. Gray & R. Struckmeyer (2008) Verification of the VARSKIN beta skin dose calculation computer code. *Health physics*, 94, 527-38.
- Siegel, J. A. & M. G. Stabin (1994) Absorbed fractions for electrons and beta particles in spheres of various sizes. *Journal of nuclear medicine : official publication, Society of Nuclear Medicine*, 35, 152-6.
- Smits, M. L., J. F. Nijsen, M. A. van den Bosch, M. G. Lam, M. A. Vente, W. P. Mali, A. D. van Het Schip & B. A. Zonnenberg (2012) Holmium-166 radioembolisation in patients with unresectable, chemorefractory liver metastases (HEPAR trial): a phase 1, dose-escalation study. *The Lancet. Oncology*, 13, 1025-34.
- Song, S. Y., J. W. Chung, Y. H. Yin, H. J. Jae, H. C. Kim, U. B. Jeon, B. H. Cho, Y. H. So & J. H. Park (2010) Celiac axis and common hepatic artery variations in 5002 patients: systematic analysis with spiral CT and DSA. *Radiology*, 255, 278-88.
- Spreatico, C., M. Maccauro, V. Mazzaferro & C. Chiesa (2014) The dosimetric importance of the number of ⁹⁰Y microspheres in liver transarterial radioembolization (TARE). *European journal of nuclear medicine and molecular imaging*, 41, 634-8.
- Stabin, M. G., K. F. Eckerman, J. C. Ryman & L. E. Williams (1994) Bremsstrahlung radiation dose in yttrium-90 therapy applications. *Journal of nuclear medicine : official publication, Society of Nuclear Medicine*, 35, 1377-80.
- Stenvall, A., E. Larsson, S. E. Strand & B. A. Jönsson (2014) A small-scale anatomical dosimetry model of the liver. *Physics in medicine and biology*, 59, 3353-71.
- Strigari, L., R. Sciuto, S. Rea, L. Carpanese, G. Pizzi, A. Soriani, G. Iaccarino, M. Benassi, G. M. Ettorre & C. L. Maini (2010) Efficacy and toxicity related to treatment of hepatocellular carcinoma with

- 90Y-SIR spheres: radiobiologic considerations. Journal of nuclear medicine : official publication, Society of Nuclear Medicine, 51, 1377-85.*
- Teutsch, H. F. (2005) *The modular microarchitecture of human liver. Hepatology, 42, 317-25.*
- Tveit, E., L. Weiss, S. Lundstam & R. Hultborn (1987) *Perfusion characteristics and norepinephrine reactivity of human renal carcinoma. Cancer Research, 47, 4709-13.*
- Uusijärvi, H., P. Bernhardt, F. Rosch, H. R. Maecke & E. Forssell-Aronsson (2006) *Electron- and positron-emitting radiolanthanides for therapy: aspects of dosimetry and production. Journal of nuclear medicine : official publication, Society of Nuclear Medicine, 47, 807-14.*
- Walrand, S., M. Hesse, C. Chiesa, R. Lhommel & F. Jamar (2014a) *The low hepatic toxicity per Gray of 90Y glass microspheres is linked to their transport in the arterial tree favoring a nonuniform trapping as observed in posttherapy PET imaging. Journal of nuclear medicine : official publication, Society of Nuclear Medicine, 55, 135-40.*
- Walrand, S., M. Hesse, G. Demonceau, S. Pauwels & F. Jamar (2011) *Yttrium-90-labeled microsphere tracking during liver selective internal radiotherapy by bremsstrahlung pinhole SPECT: feasibility study and evaluation in an abdominal phantom. EJNMMI research, 1, 32.*
- Walrand, S., M. Hesse, F. Jamar & R. Lhommel (2014b) *A Hepatic Dose-Toxicity Model Opening the Way Toward Individualized Radioembolization Planning. Journal of nuclear medicine : official publication, Society of Nuclear Medicine, 55, 1317-1322.*
- van de Maat, G. H., P. R. Seevinck, M. Elschot, M. L. Smits, H. de Leeuw, A. D. van Het Schip, M. A. Vente, B. A. Zonnenberg, H. W. de Jong, M. G. Lam, M. A. Viergever, M. A. van den Bosch, J. F. Nijsen & C. J. Bakker (2013) *MRI-based biodistribution assessment of holmium-166 poly(L-lactic acid) microspheres after radioembolisation. European radiology, 23, 827-35.*
- Van de Wiele, C., A. Maes, E. Brugman, Y. D'Asseler, B. De Spiegeleer, G. Mees & K. Stellamans (2012) *SIRT of liver metastases: physiological and pathophysiological considerations. European journal of nuclear medicine and molecular imaging, 39, 1646-55.*
- Vente, M. A., M. Wondergem, I. van der Tweel, M. A. van den Bosch, B. A. Zonnenberg, M. G. Lam, A. D. van Het Schip & J. F. Nijsen (2009) *Yttrium-90 microsphere radioembolization for the treatment of liver malignancies: a structured meta-analysis. European radiology, 19, 951-9.*
- Wissmeyer, M., S. Heinzer, P. Majno, F. Buchegger, H. Zaidi, V. Garibotto, M. Viallon, C. D. Becker, O. Ratib & S. Terraz (2011) *(9)(0)Y Time-of-flight PET/MR on a hybrid scanner following liver*

- radioembolisation (SIRT). European journal of nuclear medicine and molecular imaging, 38, 1744-5.*
- Wongergem, M., M. L. Smits, M. Elschot, H. W. de Jong, H. M. Verkooijen, M. A. van den Bosch, J. F. Nijssen & M. G. Lam (2013) *99mTc-macroaggregated albumin poorly predicts the intrahepatic distribution of 90Y resin microspheres in hepatic radioembolization. Journal of nuclear medicine : official publication, Society of Nuclear Medicine, 54, 1294-301.*
- Wu, J. (2004) *Effects of changing scale on landscape pattern analysis: scaling relations. Landscape Ecology, 19, 125-138.*
- Yip, D., R. Allen, C. Ashton & S. Jain (2004) *Radiation-induced ulceration of the stomach secondary to hepatic embolization with radioactive yttrium microspheres in the treatment of metastatic colon cancer. Journal of gastroenterology and hepatology, 19, 347-9.*